

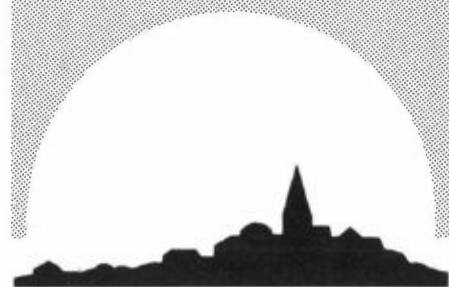
NILU TR: 2/87

NILU TR : 2/87  
REFERENCE: E-8263  
DATE : JUNE 1987  
ISBN : 82-7247-813-7

A NUMERICAL MODEL SUITABLE FOR  
THE SIMULATION OF A BROAD CLASS  
OF CIRCULATION SYSTEMS ON THE  
ATMOSPHERIC MESOSCALE

Trond Iversen and Thor Erik Nordeng\*

\* The Norwegian Meteorological Institute  
P.O.Box 43 Blindern, 0313 OSLO 3



**NILU**

NORSK INSTITUTT FOR LUFTFORSKNING  
Norwegian Institute For Air Research  
POSTBOKS 64 — N-2001 LILLESTRØM — NORWAY

## PREFACE

The Norwegian Institute for Air Research (NILU) and the Norwegian Meteorological Institute (DNMI) has cooperated in developing a numerical model for calculation of atmospheric flows on the mesoscale. The base of the model is the adiabatic part of the numerical weather prediction model at DNMI. The model is constructed to be run on the DNMI computer system (FPS-164/IBM-4341). The cooperation between NILU and DNMI was encouraged by Professor Anton Eliassen, DNMI.



## SUMMARY

This report gives a complete description of a numerical model, constructed to simulate a wide range of flows on the atmospheric meso-scale. The adiabatic part of the model is taken from the routine weather prediction model at DNMI. The boundary layer formulation requires a dense resolution of the lower 1.5 km of the atmosphere. A first order closure scheme, which distinguishes between the unstable and the stable boundary layer, is chosen. Topography is included by using terrain-following coordinate surfaces, combined with a staggering of the vertical grid which lead to a consistent computation of the horizontal pressure forces. The physical processes include precipitation and clouds, terrestrial radiation and an equation for ground surface temperature. The sea surface temperature must be prescribed. The lateral boundary conditions is a relaxation-zone scheme modified to take into account effects of physical forcing. In all tested cases it has performed excellently. Since the model is quasi-hydrostatic, a lower limit is imposed on the scales to be simulated. It is recommended that the grid resolution is 1 km or larger when simulating slow wind speed situations with a strong static stability. When modelling general mesoscale structures, the grid increment should be 5 km or larger. The few tests made so far are promising, but more case studies remain to be made.



## CONTENTS

	Page
PREFACE .....	1
SUMMARY .....	3
1 INTRODUCTION .....	7
2 BASIC EQUATIONS AND NUMERICAL METHODS .....	8
3 PARAMETERIZATION OF TURBULENCE .....	12
3.1 The surface layer .....	13
3.2 The stable boundary layer .....	14
3.3 The convective boundary layer .....	16
3.4 Solution of the advection-diffusion equation .....	17
4 PARAMETERIZATION OF PHYSICAL PROCESSES .....	21
4.1 Cloud parameterization .....	21
4.2 Terrestrial radiation .....	22
4.3 Solar Radiation .....	26
4.4 Ground/sea surface equations .....	29
4.5 Condensation and precipitation .....	31
5 LATERAL BOUNDARY CONDITIONS .....	35
5.1 The relaxation scheme .....	39
5.2 Experiments on boundary conditions .....	40
5.3 Conclusive remarks on boundary conditions .....	48
6 POSSIBLE APPLICATIONS .....	48
6.1 Analytical solutions .....	49
6.1.1 Free waves .....	49
6.1.2 Forced waves .....	52
6.1.3 Forced circulation .....	52
6.1.4 Unstable atmosphere .....	53
6.2 A scale analysis .....	54
7 EXAMPLES OF APPLICATION .....	56
7.1 Coastal circulation .....	56
7.2 Gauss-mountain .....	57
7.3 Complex topograhpy .....	61
8 REFERENCES .....	61



## 1 INTRODUCTION

The first three-dimensional, mesoscale models were made to study sea breezes along coastal shores (McPherson, 1970; Pielke, 1974; Tapp and White, 1976). These models did not contain a complete description of physical processes within the atmosphere, but was constructed for case studies. Later, more complete physical schemes were incorporated into the models, which thus had a much wider area of application (Anthes and Warner, 1978; Carpenter, 1979). Subsequent to these pioneering papers, the research on the atmospheric mesoscale has intensified considerably. This is very much due to the invention of larger and faster computers, but is probably also a consequence of new ways of taking observations, especially by means of weather radars. The new discipline in modern weather prediction called "now casting", requires detailed knowledge of wind and precipitation in complex topography and coastal areas. There is also severe weather related to mesoscale vortices (tropical cyclones, polar lows) and unstable zones (cold fronts, squall lines).

Another area of application is air quality modelling. Such modelling on scales from local to regional, requires detailed knowledge of wind and turbulence. During episodes of high concentrations of pollutants, winds and turbulence are very often weak and dominated by mesoscale forcing.

This report describes a numerical model for simulation of atmospheric flows on the mesoscale. It includes a wide range of processes, which makes it quite generally applicable. The main restriction of the applicability is the use of the quasihydrostatic approximation. This approximation simplifies the numerical integration considerably, since vertically propagating, acoustic waves are removed. However, it restricts the model to simulations on scales larger than a certain minimum. After the general model descriptions in sections 2,3,4 and 5, the limitation of its applicability due to the quasihydrostatic approximation is summarized in section 6. Section 7 concludes the report with a few preliminary examples.



## 2 BASIC EQUATIONS AND NUMERICAL METHODS

The adiabatic part of the model is the same as used in the routine numerical weather prediction model at The Norwegian Meteorological Institute (Grønås and Hellevik, 1982). The vertical coordinate is normalized pressure ( $\sigma$ ) with an upper lid at the constant pressure level  $p = p_T$ , i.e.

$$\sigma = \frac{p - p_T}{p_S - p_T} \quad (2.1)$$

where  $p_S$  is the pressure on the ground surface. The horizontal coordinates are cartesian, and the quasi-hydrostatic approximation is assumed to be valid. The governing equations on a conformal map with transformation factor  $m$  and  $\vec{v} = (u, v)$  is the wind divided by  $m$ , are the hydrostatic equation

$$\varphi_\sigma + e\Pi_\sigma = 0, \quad (2.2)$$

the continuity equation

$$(p_S)_t + m^2 \vec{\nabla} \cdot (p_* \vec{v}) + (\dot{p}_*)_\sigma = 0, \quad (2.3)$$

the horizontal equations of motion

$$\begin{aligned} u_t + m^2 \vec{\nabla} \cdot \nabla u + m \vec{v}^2 m_x + \dot{u}_\sigma &= fv - \varphi_x - e\Pi_x + (u_t)_{\text{eddy}} \\ v_t + m^2 \vec{\nabla} \cdot \nabla v + m \vec{v}^2 m_y + \dot{v}_\sigma &= -fu - \varphi_y - e\Pi_y + (v_t)_{\text{eddy}}, \end{aligned} \quad (2.4)$$

the thermodynamic energy equation

$$e_t + m^2 \vec{\nabla} \cdot \nabla e + \dot{e}_\sigma = (e_t)_{\text{eddy}} + (e_t)_{\text{rad}} + (e_t)_{\text{lat}}, \quad (2.5)$$

the equation for water vapor

$$q_t + m^2 \vec{\nabla} \cdot \nabla q + \dot{q}_\sigma = (q_t)_{\text{phase}} + (q_t)_{\text{eddy}}. \quad (2.6)$$

Here  $\Pi = c_p(p/p_0)^{R/c_p}$  is the Exner function,  $\dot{\sigma} = d\sigma/dt$  and  $p_* = p_S - p_T$ .

All quantities are ensemble averages, i.e. the system is purely deterministic. Tendencies subscribed by "eddy" are deterministic terms due to nonlinear interaction between stochastic fluctuations. The terms  $(e_t)_{\text{rad}}$  and  $(e_t)_{\text{lat}}$  are diabatic heating due to long wave radiation and condensation of water vapor respectively, while  $(q_t)_{\text{phase}}$  is the evaporation rate. The humidity's impact on buoyancy is not taken into account, since the specific humidity is assumed to be small. If necessary, however, it could be taken into account by computing the virtual, potential temperature  $e_v = [1 + (\frac{1}{\epsilon} - 1)q]e$ , where  $\epsilon \approx 5/8$ .

The upper and lower, kinematic boundary conditions imply

$$\dot{\sigma} = d\sigma/dt = 0 \text{ for } \sigma = 0 \text{ and } \sigma = 1 \quad (2.7)$$

The upper condition is an approximation when  $p_T > 0$  since  $p_T$  is a temporal constant. The part of the atmosphere with  $p \in [0, p_T]$  is implicitly assumed to be at rest. If  $p_T$  is chosen to be above the tropopause, this approximation is not expected to cause significant errors for short term prognostic calculations. However, this condition may cause spurious reflections of vertically propagating waves.

The independent variables are  $x, y, \sigma$  and  $t$ . The system is posed as an initial-boundary value problem in the dependent variables  $u, v, e, q$  and  $p_s$ . All these variables are ideally supposed to be known for all points  $(x, y, \sigma)$  inside a simply connected region for  $t = 0$  (initially) and at its boundary for  $t > 0$ . The problem is then to find the variables within the region for  $t > 0$ .

With  $p_s$  and  $e$  known,  $p$  (and hence  $\Pi$ ) is calculated from (2.1) and  $\varphi$  by integrating (2.2):

$$\varphi = \varphi_s + \int_{\Pi}^{\Pi} e \delta \Pi \quad (2.8)$$

where  $\varphi_s$  is the surface geopotential (i.e. the topography). By integrating (2.3) vertically,  $(p_s)_t$  is found from

$$(p_s)_t = -m^2 \int_0^1 \nabla \cdot (p_* \vec{v}) \delta \sigma \quad (2.9)$$

where (2.7) has been applied. The "vertical" motion  $\dot{\sigma}$  is also found from (2.3):

$$\dot{\sigma} = - \frac{1}{p_{* \sigma}} \left[ (p_s)_t \sigma + m^2 \int_0^\sigma \nabla \cdot (p_* \vec{v}) \delta \sigma \right] \quad (2.10)$$

With the eddy- and forcing-terms known,  $u_t$ ,  $v_t$ ,  $e_t$  and  $q_t$  are determined from (2.4), (2.5) and (2.6).

One major problem that arises when integrating the primitive equations with coordinate surfaces not being close to horizontal, is the calculation of the horizontal pressure force. When the coordinate surface slopes, this force show up as a small difference between two large terms. In the present model, a vertically staggered discretization has been chosen in order to arrive at a consistent approximation to the horizontal pressure force (Janjic, 1977), see Fig. 2.1.

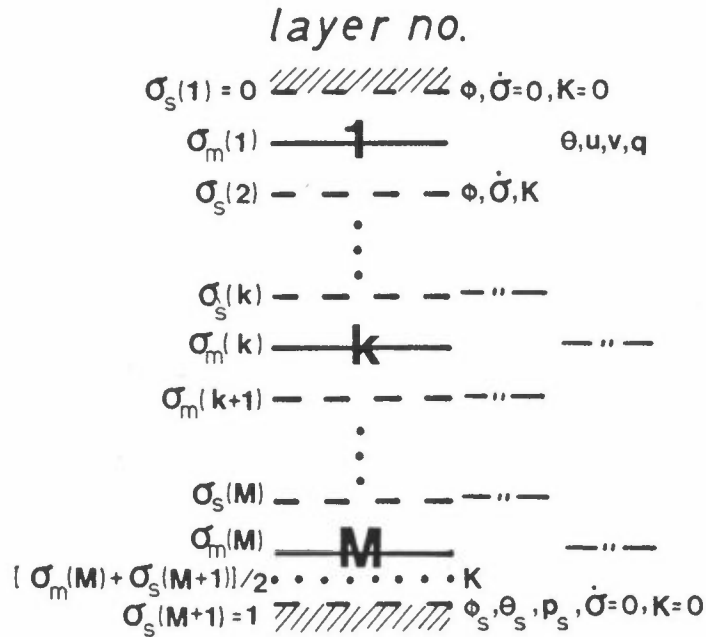


Figure 2.1: The vertical staggering of variables in the model.

However, a consistent approximation, in the sense that the finite difference expression converges towards the differential operator as the grid increment becomes infinite simally small, does not eliminate truncation errors. The net horizontal pressure force is calculated by the difference between the gravity force and total pressure force projected onto the coordinate surface  $\sigma = \text{const}$ . The major part of

these terms cancel due to the quasi-hydrostatic assumption. Since the horizontal grid resolution normally is several orders of magnitude coarser than the vertical, the hydrostatic balance that is approximated when calculating the horizontal pressure force has much larger truncation error than the balance approximated when integrating the vertical hydrostatic equation (2.8). This causes errors that will increase with height since (2.8) is cumulative. On the mesoscale, the largest errors will be expected to show up in the mass field, since an imbalance on this scale will cause the mass field to adjust towards the wind field (e.g. Økland, 1972). The problem to calculate the horizontal pressure force has been addressed by several authors (e.g. Sundqvist, 1975; Janjic, 1977; Mesinger and Janjic, 1983).

The horizontal, finite difference scheme is one of the schemes presented by Bratseth (1983). It combines the accuracy of a timestaggered D-grid (Eliassen-grid, see Fig. 2.2) with the advantages of a scheme that is not staggered in time. The combination is made possible by means of a third order accurate interpolation. A variable, e.g.  $e$ , is discretized in a uniform, square grid on a conformal map. Preliminary tendencies are computed in the centres of each grid square, and interpolated, accurately to the third order in grid distance  $d$ , back to the  $e$ -positions.

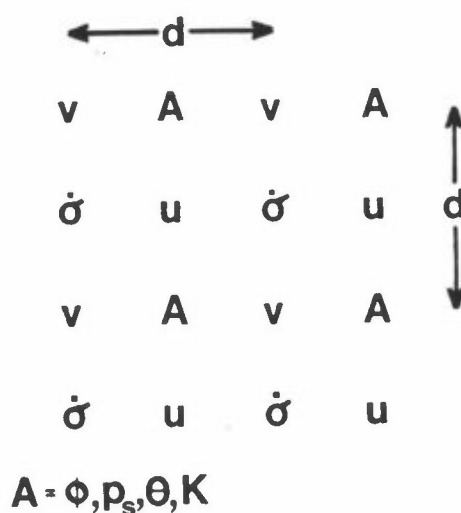


Figure 2.2: The horizontal staggering of variables in the model.

By obtaining this non-staggered (in time) scheme, the leapfrog time-integration scheme can be modified by the "Schuman pressure gradient averaging technique" with the computational mode controlled by a time-averaging filter (Brown and Campana, 1978). This implies that the time-step  $\Delta t$  can be increased with about a factor two as compared to the pure leapfrog scheme. The accurate, horizontal interpolation of tendencies also leads to a possible increase in timestep of a factor 1.5-2. The linear stability criterion is

$$\Delta t < \alpha_p \frac{d}{m \sqrt{2(c + U_{MAX})}} \quad (2.11)$$

where  $\alpha_p \in \langle 3, 4 \rangle$ ,  $U_{MAX}$  is maximum advective speed and  $c$  is the phase speed of the fastest moving horizontal waves in the system. The phase speed of Lamb waves is  $c_o \sqrt{c_p/c_v}$ , where  $c_o$  is the phase speed of external gravity waves and  $c_p$  and  $c_v$  are the specific heat of dry air at constant pressure and volume respectively.

A detailed presentation of the finite difference equations and the numerical methods is given in Grønås and Hellevik (1982).

To assure a certain balance between the mass- and wind-fields initially, a dynamic initialization scheme of the Bratseth (1982)-type is applied.

### 3 PARAMETERIZATION OF TURBULENCE

The governing equations are deterministic in the ensemble-averaged variables. Nevertheless, the nonlinearity of the system implies that stochastic energy may combine to deterministic energy. For a specified realization of the system, a quantity  $A$  may be written as a sum

$$A = \langle A \rangle + A' \quad (3.1)$$

of its ensemble average  $\langle A \rangle$  (average over an infinite number of realizations) and its stochastic deviation  $A'$ . In turbulent motion, which is common in the atmospheric boundary layer, the stochastic part of the flow is of major importance and deterministic terms that are functionals of the fluctuations (eddy-terms) are large. The model

expresses eddy-terms as functionals of the ensemble-averaged quantities through diagnostic relations (first order closure). Horizontal turbulence is assumed negligible as compared to vertical, and density fluctuations are ignored. The eddy-terms of eqs. (2.4)-(2.6) are thus

$$(A_t)_{\text{eddy}} = - \frac{g}{p_*} (-\rho \langle A' w' \rangle) \quad (3.2)$$

where  $\rho$  is density and  $w'$  is the fluctuation of vertical velocity.

The basic philosophy behind the chosen boundary layer turbulence scheme, is to treat turbulent effects locally under stable conditions and as bulk effects in the unstable regime. This is justified by the fact that the average size of the individual turbulent eddies (the mixing length) increase abruptly when the atmosphere turns unstable.

### 3.1 THE SURFACE LAYER

The surface layer can be defined as the lowermost layer in the atmosphere where the timescale is so short that the immediate adjustment approximation is valid. The turbulent flux densities are therefore constant within this layer. The sign of the vertical, turbulent heat flux density determines whether the planetary boundary layer is to be treated with local relations or with bulk formulae.

The constant surface layer flux densities is defined by  $u_*$ ,  $e_*$  and  $q_*$  through

$$\begin{aligned} u_* &= |\langle \vec{v} w' \rangle|^{1/2} \\ u_* e_* &= - \langle e' w' \rangle \\ u_* q_* &= - \langle q' w' \rangle \end{aligned} \quad (3.3)$$

To express these quantities with deterministic variables the flux-profile relationship given by Businger (1973) as a result of a boundary layer experiment (Businger et al., 1971), are used. These are, however, implicit formulae and iterative methods have often been

applied. Louis (1979) fitted explicit relations to the Businger functions, and they are used here. The Louis functions are (all heights,  $z$ ,  $h_s$ ,  $z_i$ , are relative to the ground, e.g.  $z = (\varphi - \varphi_s)/g$ ):

$$u_*^2 = a^2 |\vec{v}|^2 F_M(z/z_O, Ri_B) \quad (3.4)$$

$$u_* e_* = a^2 |\vec{v}| (e - e_s) F_H(z/z_O, Ri_B)/0.74 \quad (3.5)$$

$$u_* q_* = a^2 |\vec{v}| (q - q_s) F_H(z/z_O, Ri_B)/0.74 \quad (3.6)$$

where the bulk Richardson number is

$$Ri_B = gh_s (e(h_s) - e_s) / (e \cdot |\vec{v}|^2) \quad (3.7)$$

and  $h_s$  is the height of the surface layer. The determination of  $e_s$  and  $q_s$  is given in section 4. Furthermore,  $a^2 = k^2 \left[ \ln \frac{z}{z_O} \right]^{-2}$ ,

$$F_{M,H} = \begin{cases} 1 - \frac{2b Ri_B}{1+c|Ri_B|^{1/2}} & ; Ri_B \leq 0 \\ [1 + b Ri_B]^{-2} & ; Ri_B > 0 \end{cases} \quad (3.8)$$

and

$$c = a^2 b \sqrt{z/z_O} \cdot \begin{cases} 7.4 \text{ for } F_M \\ 5.3 \text{ for } F_H \end{cases} \quad (3.9)$$

Here  $b = 4.7$ ,  $z_O$  is the roughness length and  $k = 0.35$  (Businger et al., 1971) is the von Karman constant. The height  $h_s$  is taken to be 4% of the height  $z_i$  of the total atmospheric boundary layer, defined as the height of the lowermost layer at least 200 m above the ground where  $e(z_i) \geq e_s + \Delta e$ . We have chosen  $\Delta e = 0.2$  K.

### 3.2 THE STABLE BOUNDARY LAYER

The atmospheric boundary layer is defined as stable as a whole when  $e_* > 0$ . However, local unstable layers are possible. Traditional K-theory (the exchange hypothesis) applied to the vertical, turbulent flux density of a quantity A, give

$$\langle A'w' \rangle = - K^{(z)} A_z = \frac{g}{p_*} \rho K^{(z)} A_{\sigma}, \quad (3.10)$$

and hence from (3.2)

$$(A_t)_{\text{eddy}} = \frac{g^2}{p_*^2} (\rho^2 K^{(z)} A_{\sigma})_{\sigma}. \quad (3.11)$$

Superscript  $(z)$  denotes a quantity defined with  $z$  as vertical coordinate. To account for a counter-gradient, turbulent heat flux in weakly stable conditions (Deardorff, 1966), the eddy-term for  $e$  is slightly modified by introducing  $\gamma_{cg}^{(z)}$ :

$$(e_t)_{\text{eddy}} = \frac{g^2}{p_*} [\rho^2 K^{(z)} (e_{\sigma} + \gamma_{cg}^{(z)} \frac{p_*}{\rho g})]_{\sigma} \quad (3.12)$$

where

$$\gamma_{cg}^{(z)} = 0.7 \cdot 10^{-3} \text{ Km}^{-1}.$$

For calculation of the exchange coefficients for momentum  $K_M^{(z)}$  and heat  $K_H^{(z)}$ , formulae which are based on the Mellor and Yamada (1974) level 2-scheme are used. Formulae of the type  $K = \nu^2 |\vec{v}_z| F(\text{Ri})$  was derived by Blackadar (1979), and will be used in the present model, only slightly modified to be a continuous functions of Ri. The mixing length  $\nu$  is not determined by the Mellor and Yamada theory, and is a major problem in atmospheric turbulence theory. Here, the simple formulae used by McNider and Pielke (1981) is applied,

$$\nu = \begin{cases} kz & ; z \leq z_m \\ kz_m & ; z > z_m \end{cases} \quad (3.13)$$

where  $z_m = 200$  m. The formulae are

$$\frac{K_H^{(z)}}{\nu^2 |\vec{v}_z|} = \begin{cases} (1.1 - 87 \text{ Ri})^{1/2} & ; \text{Ri} \leq 0 \\ 1.1 - 1.2 \frac{\text{Ri}}{\text{Ri}_c} & ; 0 < \text{Ri} \leq \frac{1}{2} \text{Ri}_c \\ 1 - \frac{\text{Ri}}{\text{Ri}_c} & ; \frac{1}{2} \text{Ri}_c < \text{Ri} < \text{Ri}_c \end{cases} \quad (3.14)$$

and for momentum

$$\frac{K_M^{(z)}}{\nu^2 |\vec{v}_z|} = \begin{cases} (1 - 21 \text{ Ri})^{1/2} & ; \text{Ri} \leq 0 \\ 1 - \frac{\text{Ri}}{\text{Ri}_c} & ; 0 < \text{Ri} < \text{Ri}_c \end{cases} \quad (3.15)$$



For  $Ri \geq Ri_c$ , there is no vertical turbulent exchange. The  $Ri$ - and  $Ri_c$ -numbers are the Richardson number ( $Ri = g\theta_z/\rho|\vec{v}_z|^2$ ) and the critical Richardson number. From theory (e.g. Drazin and Howard, 1966), stratified shear flow stays laminar as long as the Richardson number is greater than 0.25. In a discretized model overturning to turbulence may be possible also for  $Ri$  somewhat larger, since the value computed by the model must be considered as a layer bulk value. Local values within a model layer can still be smaller than 0.25. On the other hand, turbulence does not necessarily occur for  $Ri < 0.25$  since this is not a sufficient condition. The formulae suggested by McNider and Pielke (1981) is used,

$$Ri_c = A \left(\frac{\Delta z}{\Delta z_0}\right)^B \quad (3.16)$$

where  $A = 0.115$ ,  $B = 0.175$ ,  $\Delta z$  is the model layer thickness and  $\Delta z_0 = 10^{-2}$  m.

### 3.3 THE CONVECTIVE BOUNDARY LAYER

The profile formulae for the exchange coefficients used when the surface layer heat flux is directed upwards, is the O'Brien (1970)-relation. Hence for  $e_* < 0$ ,

$$K = \begin{cases} \frac{z}{h_s} K(h_s) & ; z < h_s \\ K(z_i) + \left(\frac{z_i - z}{z_i - h_s}\right)^2 \{K(h_s) - K(z_i) + (z - h_s)[K_z(h_s) + 2 \frac{K(h_s) - K(z_i)}{z_i - h_s}]\} & ; h_s \leq z < z_i \end{cases} \quad (3.17)$$

where  $K$  is either  $K_M^{(z)}$  or  $K_H^{(z)}$ .

Above the convective boundary layer ( $z \geq z_i$ ) the formulae (3.14) and (3.15) are applied. Since the surface layer flux densities are already known, the Businger et al. (1971)-functions can be used explicitly to find  $K(h_s)$  and  $K_z(h_s)$ . Thus

$$K_{M,H}^{(z)} = u_* k z / \Phi_{M,H} \left(\frac{z}{L}\right) \quad (3.18)$$

Where  $L = \epsilon u_*^2 / k g \epsilon_*$  is the Monin-Obhukov length. In the unstable surface layer,

$$\Phi_M = (1 - 15 z/L)^{1/4} \quad (3.19)$$

and

$$\Phi_H = 0.74 / (1 - 9 z/L)^{1/2} \quad (3.20)$$

In the free convection limit ( $\epsilon_* < 0$  and  $u_* \rightarrow 0$ ) (3.20) cannot be used. To be able to include also such cases, one assumes

$$\Phi_H = 0.74 / (1 - \alpha z/L)^{1/3} \quad ; \quad z/L \leq -2 \quad (3.21)$$

Demanding continuity for  $z/L = -2$ , one arrives at

$$\alpha = \frac{1}{2} (\sqrt{6859} - 1) \approx 40.9. \quad (3.22)$$

The free convection limit of  $K_H^{(z)}$  is then

$$K_H^{(z)}(u_* \rightarrow 0) = (\alpha k a^2 b / 0.74 c)^{1/3} (k g z^2 / 0.74 \epsilon) | \epsilon(h_s) - \epsilon_s |^{1/2} \quad (3.23)$$

$K(h_s)$  is found by entering  $z = h_s$  in (3.18) and the gradient  $K_z(h_s)$  by differentiating (3.18) with respect to  $z$  and entering  $z = h_s$ .

### 3.4 SOLUTION OF THE ADVECTION-DIFFUSION EQUATION

The prognostic equations (2.4), (2.5) and (2.6) are parabolic differential equations that contain terms of the advective and diffusive type. These two kinds of terms possess significantly different properties with respect to numerical approximations. Discretizations which are stable under certain conditions for one of the terms, are unconditionally unstable for the other. The numerical integration of the governing equations therefore needs considerable concern.

Since advective terms corresponds to oscillation and diffusive terms to damping, the linear numerical properties of the time integration may be studied in full generality by the equation

$$A_t = -i\omega A - \kappa^2 A \quad (3.24)$$

where  $\omega$  and  $\kappa$  are real numbers and  $i$  is the imaginary unit. The equation can be interpreted as governing the time development of the eigenfunctions  $A$  in a linear system, with  $\omega$  being the eigenvalues for the oscillatory terms and  $\kappa^2$  the eigenvalues for the damping terms. As an example, consider the equation  $h_t = -Uh_x + Kh_{zz}$ . Introducing the Fourier component  $h = A \exp[i(kx + mz)]$  lead to (3.24) with  $\omega = Uk$  and  $\kappa^2 = Km^2$ .

To be able to solve the advection-diffusion equation numerically, a fully implicit (backward) scheme is used for the diffusion terms and a conditionally stable, explicit three-level scheme for the oscillation terms (Bratseth, 1983).

The diffusive step is first made:

$$A^* = A^{(n-1)} - \kappa^2 \Delta t A^*$$

giving

$$A^* = A^{(n-1)} / (1 + 2\Delta t \kappa^2),$$

where  $n$  denotes the time level and the asterics a preliminary value of  $A^{(n+1)}$ . By approximating

$$(-\kappa^2 A^{(n)}) \approx (A^* - A^{(n-1)}) / \Delta t = \kappa^2 A^{(n-1)} / (1 + 2\Delta t \kappa^2),$$

and using the leap frog scheme for the oscillation term, one arrives at

$$A^{(n+1)} = A^{(n-1)} - i2\Delta t \omega A^{(n)} - \frac{2\Delta t \kappa^2}{1 + 2\Delta t \kappa^2} A^{(n-1)} \quad (3.25)$$

Assuming  $A^{(n)} = \lambda^n A^{(0)}$  where  $\lambda$  is constant, one gets

$$\lambda_{\pm} = i\omega \Delta t \pm [1 / (1 + 2\Delta t \kappa^2) - \omega^2 \Delta t^2]^{1/2} \quad (3.26)$$

The von Neuman sufficient condition for stability is that  $|\lambda| \leq 1$ . Now,

$$|\lambda_{\pm}|^2 = \begin{cases} 1/(1+2\Delta t \kappa^2) & ; \omega^2 \Delta t^2 \leq 1/(1+2\Delta t \kappa^2) \\ \{\omega \Delta t \mp [\omega^2 \Delta t^2 - 1/(1+2\Delta t \kappa^2)]^{1/2}\}^2 & ; \omega^2 \Delta t^2 > 1/(1+2\Delta t \kappa^2) \end{cases}$$

The solution  $\lambda_+$  corresponds to the physical situation and is always stable, since  $|\lambda_+| \leq 1$  for all  $\omega$  and  $\kappa$ . However, the spurious part of the solution (normally called the computational mode) ruins the unconditional stability. The instability increases with increasing damping factor  $\kappa^2$ , and when  $\kappa^2 \rightarrow \infty$ , then  $|\lambda_-| \rightarrow 2|\omega|\Delta t$ . Hence, the linear stability criterion is

$$|\omega|\Delta t \leq 1/2 \quad (3.27)$$

Consequently, to achieve a stable integration for all possible values of  $\kappa$  and  $\omega$ , the timestep must be half the one required with no diffusion terms. Thus, the stability criterion (2.11) is to be applied with  $\alpha_p \in \langle 1.5, 2 \rangle$ .

In practice when applying the fully implicit scheme on the diffusion equation, a set of simultaneous linear equations have to be solved in order to compute the preliminary fields for timelevel (n+1). The diffusion equations take the form

$$A_t = [K(A_\sigma - \gamma)]_\sigma \quad (3.28)$$

where A is either u, v, e or q, the countergradient flux density is zero unless A=e, and  $K = g^2 p^2 K^{(z)}/p_*^2$ . Following the notation of Figure 2.1, the finite difference version of (3.28) is

$$A_k^{(n+1)} = A_k^{(n-1)} + \frac{2\Delta t}{\sigma_S(k+1) - \sigma_S(k)} \left[ K_{k+1} \frac{A_{k+1}^{(n+1)} - A_k^{(n+1)}}{\sigma_M(k+1) - \sigma_M(k)} - K_k \frac{A_k^{(n+1)} - A_{k-1}^{(n+1)}}{\sigma_M(k) - \sigma_M(k-1)} - K_k \frac{A_k^{(n+1)} - A_{k-1}^{(n+1)}}{\sigma_M(k) - \sigma_M(k-1)} - \gamma(K_{k+1} - K_k) \right] \quad (3.29)$$

for  $k \in \{2, \dots, K_M - 1\}$

The boundary conditions are for  $k=1$ :

$$A_1^{(n+1)} = A_1^{(n-1)} + \frac{2\Delta t}{\sigma_S(2) - \sigma_S(1)} \left[ K_2 \frac{A_2^{(n+1)} - A_1^{(n+1)}}{\sigma_M(2) - \sigma_M(1)} - \gamma K_2 \right], \quad (3.30)$$

and for  $k=K_M$ :

$$A_{K_M}^{(n+1)} = A_{K_M}^{(n-1)} + \frac{2\Delta t}{[\sigma_S(K_S) + \sigma_M(K_M)]/2 - \sigma_S(K_M)} \cdot \left[ K_{K_S} \frac{A_{K_S}^{(n+1)} - A_{K_M}^{(n+1)}}{\sigma_S(K_S) - \sigma_M(K_S)} - K_{K_M} \frac{A_{K_M}^{(n+1)} - A_{K_M-1}^{(n+1)}}{\sigma_M(K_M) - \sigma_M(K_M-1)} - \gamma(K_{K_S} - K_{K_M}) \right] \quad (3.31)$$

The surface values are

$$A_{K_S}^{(n+1)} = \begin{cases} 0 & ; A=u, v \\ e_{K_S}^{(n-1)} + 2\Delta t (e_{K_S})_t^{(n-1)} & ; A = e \\ \alpha q_{\text{sat}}(p_{K_S}^{(n+1)}, T_{K_S}^{(n+1)}) + (1-\alpha) q_{K_M}^{(n+1)} & ; A = q \end{cases} \quad (3.32)$$

The formula for  $A = q$  is explained in section 4 (eq. (4.17)); the factor  $\alpha \in [0,1]$  is a measure of the available ground surface humidity. In summary, the equations (3.29) through (3.32) may be written as a three-level recursion formula

$$-\tau_{k-1} A_{k-1}^{(n+1)} + \beta_k A_k^{(n+1)} - \tau_k A_{k+1}^{(n+1)} = H_k \quad (3.33)$$

for  $k \in \{1, \dots, K_M\}$ ; where  $\tau_0 = 0$ ,  $\tau_k$ ,  $\beta_k$  and  $H_k$  are known for  $k \in \{1, \dots, K_M\}$ , and  $A_{K_S}^{(n+1)}$  is known.

This recursion formula is solved for  $A_k^{(n+1)}$  by Gauss-elimination (Potter, 1973).

## 4 PARAMETERIZATION OF PHYSICAL PROCESSES

The physical processes that are implemented in the model include terrestrial and solar radiation, condensation processes, and cloud parameterization. Furthermore, there are two methods for calculation of ground surface temperature and a simple method for calculation of ground surface moisture. This comes in addition to the turbulence parameterization which is described in section 3.

### 4.1 CLOUD PARAMETERIZATION

Fractional cloud cover to be used in the radiation scheme is taken as a function of relative humidity:

$$a = \left( \max \left\{ \frac{U - U_c}{1 - U_c}, 0 \right\} \right)^2 \quad (4.1)$$

where  $U$  is relative humidity and  $U_c$  is the threshold humidity for clouds to exist. Eq. (4.1) reflects that any model variable may be regarded as a mean value within a grid volume, and that subgrid scale fluctuations are possible. Even for a subsaturated model layer ( $U < 1$ ), local patches of clouds may be expected.  $U_c$  is a function of the grid distance  $d$ , and should approach unity as the resolution gets better. In the experiments reported here, we have chosen  $U_c = 0.8$  for all kinds of clouds in the free atmosphere, and  $U_c = 0.92$  for boundary layer clouds (fog). In the unstable boundary layer, clouds are not supposed to exist even if the relative humidity would allow it. Thus we put  $a = 0$  if the surface layer heat flux density is directed upwards.

The long-wave radiation scheme assumes clouds to be black body radiators. This is not correct for cloud depths less than ca 100 m. We have therefore chosen to have a layer thickness dependence on cloud coverage:

$$a' = a \cdot \min\{\Delta\sigma/\Delta\sigma_{cr}, 1\},$$

thus letting thin clouds act as grey radiators. At standard atmospheric pressure and temperature, 12 hPa corresponds approximately to 100 m. We therefore put  $\Delta\sigma_{cr} = 12 \text{ hPa}/p^*$ .

#### 4.2 TERRESTRIAL RADIATION

The species that are the principal absorbers and emitters of terrestrial radiation in the troposphere, are water vapour, liquid water and carbondioxide. In this scheme the emissivity approximation is used in solving the radiative transfer equation. This means that the radiative transfer equation has been integrated over frequency once and for all by defining emissivity-functions which do not depend on frequency. See Stephens (1984) for a comprehensive review on parameterization of radiation. In terms of the emissivity, the contribution to the long wave radiation flux density at a level ( $\sigma$ ) from a layer ( $\sigma'$ ) with thickness  $\Delta\sigma$  are (radiation is counted positive when directed upwards):

$$\Delta\Phi^L(\sigma) = B(T(\sigma')) \frac{dE(\sigma, \sigma')}{d\sigma'} \Delta\sigma'$$

where  $B(T(\sigma'))$  is the black body radiation flux density at temperature  $T(\sigma')$  and  $E$  is the emissivity function (see Fig. 1a). Net long wave radiation flux density at a level ( $\sigma$ ) is then found by integration over all model layers:

$$\begin{aligned} \Phi^L(\sigma) &= \int_{\sigma}^0 B(T(\sigma')) \frac{dE(\sigma, \sigma')}{d\sigma'} d\sigma' \\ &+ \int_{\sigma}^1 B(T(\sigma')) \frac{dE(\sigma, \sigma')}{d\sigma'} d\sigma' \\ &+ (1 - E(1, \sigma)) B(T_s), \end{aligned}$$

where  $T_s$  is the ground surface temperature. The emissivity function  $E$  depends on carbondioxide and water vapour:  $E(\sigma, \sigma') = E_v(\sigma, \sigma') + E_{CO_2}(\sigma, \sigma')$ .  $E_v(\sigma, \sigma')$  is given by Jacobs et al. (1974):

$$E_V(\sigma, \sigma') = \begin{cases} 0.113 \log_{10} [1 + 12.62 \zeta(\sigma, \sigma')], & \log_{10} \zeta < -4 \\ 0.104 \log_{10} (\zeta(\sigma, \sigma')) + 0.440, & -4 \leq \log_{10} \zeta < -3 \\ 0.121 \log_{10} (\zeta(\sigma, \sigma')) + 0.491, & -3 \leq \log_{10} \zeta < -1.5 \\ 0.146 \log_{10} (\zeta(\sigma, \sigma')) + 0.527, & -1.5 \leq \log_{10} \zeta < -1 \\ 0.161 \log_{10} (\zeta(\sigma, \sigma')) + 0.542, & -1 \leq \log_{10} \zeta < 0 \\ 0.136 \log_{10} (\zeta(\sigma, \sigma')) + 0.542, & \log_{10} \zeta \leq 0 \end{cases} \quad (4.2)$$

$\zeta(\sigma, \sigma')$  is the pressure corrected path length between levels ( $\sigma$ ) and ( $\sigma'$ ) (CGS- units, i.e.  $\text{g}/\text{cm}^2$ ) and is given by

$$\zeta(\sigma, \sigma') = \left| \int_{\sigma}^{\sigma'} \alpha_V \bar{\sigma}^{-1/2} p_* d\bar{\sigma} / g \right| \quad (4.3)$$

Assuming constant  $\text{CO}_2$  concentration in the atmosphere, the emissivity for carbondioxide is (Kondratyev, 1969):

$$E_{\text{CO}_2}(\sigma, \sigma') = 0.185 [1 - \exp(-0.392 C(\sigma, \sigma')^{0.4})] \quad (4.4)$$

where  $C(\sigma, \sigma') = 0.415 |p(\sigma) - p(\sigma')|$  and the pressure  $p$  is given in hPa.

When clouds are present in a model layer, the procedure is somewhat altered. Fig. 4.1b shows a principal sketch of the method.

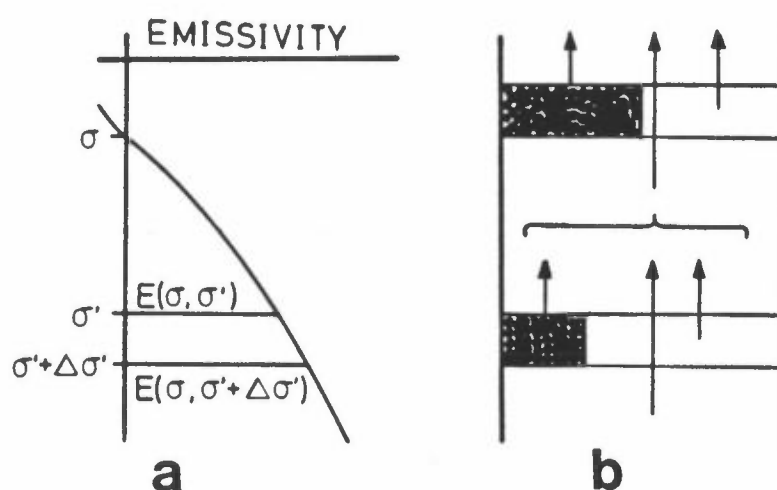


Figure 4.1: Illustration to radiation scheme.

- Sketch of how the layer between  $\sigma'$  and  $\sigma' + \Delta\sigma'$  contributes to the long wave radiation at level  $\sigma$ .  $E$  is the emissivity function.
- Sketch of how the contribution of fractional cloud cover is taken into account in the radiation scheme. Shaded areas signify clouds.



Inclusion of clouds complicates the radiative transfer equations. From Fig. 4.1 it is seen that the contribution to the long wave radiative flux density at a level  $\sigma$  from a layer of width  $\Delta\sigma'$  at a level  $\sigma'$  can be written as:

$$\begin{aligned} \Delta\phi^L(\sigma) &= a(\sigma')B(T(\sigma')) [1-E(\sigma,\sigma')] \\ &+ [1-a(\sigma')]B(T(\sigma')) \cdot [E(\sigma,\sigma'+\Delta\sigma')-E(\sigma,\sigma')] \end{aligned}$$

Contributions from layers beneath  $\sigma'$  can only pass through the cloud-free part of layer  $\Delta\sigma'$ . Downward and upward flux densities at a level  $k$  are therefore found from the summations,

$$\Phi_k^{L\downarrow} = \sum_{j=0}^{k-1} \{a_j B_s(j+1)[1-E(k,j+1)] + (1-a_j)B_m(j)[E(k,j)-E(k,j+1)]\} P_{j+1,k-1} \quad (4.5)$$

$$\Phi_k^{L\uparrow} = \sum_{j=k}^{M+1} \{a_j B_s(j)[1-E(k,j)] + (1-a_j)B_m(j)[E(k,j+1) - E(k,j)]\} P_{k,j-1}$$

where  $P_{k,j} = \prod_{i=k}^j (1-a_i)$ . If  $k > j$ , then  $P_{k,j} \equiv 1$ .

$B_m(j)$  is the black body radiative flux density at main model levels, while  $B_s(j)$  is defined at levels separating the model layers. The vertical staggering of variables for radiation calculations are given in Figure 4.2. The contribution from the atmosphere above the model is taken into account by counting it as one layer, where there is no clouds ( $a_0=0$ ) and only  $CO_2$  is creating radiation. The blackbody radiation flux density  $B_m(0)$  is the average of  $B_m(1)$  and the radiation emitted at temperature 140 K.

The temperature change in a layer due to long wave radiation is computed from the net radiation flux per unit mass,  $(\Phi^L = \Phi^L \uparrow - \Phi^L \downarrow)$

$$(\theta_t)_{\text{rad}} = \frac{g}{p_* \Pi} \frac{\partial \Phi^L}{\partial \sigma}, \text{ or in finite differences:}$$

$$((\theta_t)_{\text{rad}})_k = \frac{g}{p_* \Pi_k} \frac{\Phi_{k+1}^L - \Phi_k^L}{\sigma_{k+1} - \sigma_k} \quad (4.6)$$

The long wave radiation computations are rather time consuming and there are several possibilities to simplify the scheme. Since the computation time for the radiation in a N-layer model is proportional to N-square, one approach is to compute radiation cooling in a coarse vertical grid.

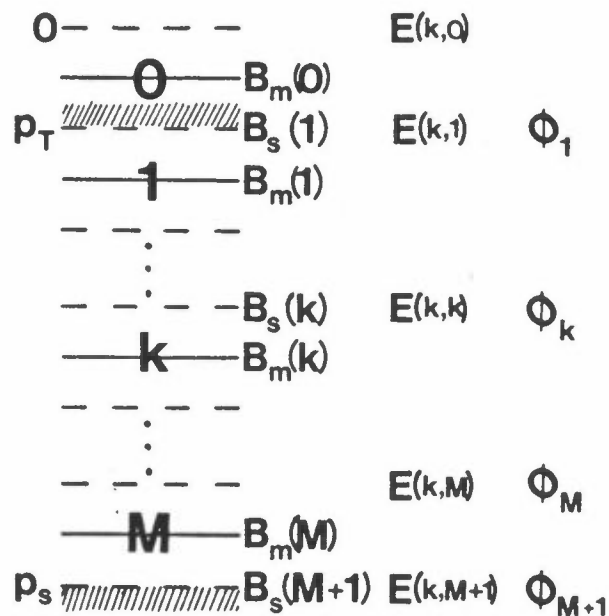


Figure 4.2: Vertical staggering of variables in the radiation calculations.

We have chosen not to compute radiation tendencies every time step. Results from the previous calculation are used until the radiation is recalculated. At present, the calculations are performed every half hour of simulation time. The long wave radiation flux densities at ground are, however, computed every time step for use in the ground surface temperature equation (Sect. 4.4).

### 4.3 SOLAR RADIATION

The short wave radiation emitted from the sun is modified in the atmosphere by scattering and absorption in clouds and clear air and varies according to geographic location and time of day and year. Absorption due to water vapour is estimated by McDonald (1960):

$$A_w(k) = 0.77(\zeta(k)\sec\alpha)^{0.3} \quad (4.7)$$

where  $\zeta(k)$  is the optical depth from the top of the atmosphere to level  $k$  (Eq. (4.3)), and  $\alpha$  is the zenith angle. Scattering in clear air is taken from Kondratyev (1969):

$$\tau(k) = 1.041 - 0.16 [0.051 + 0.949(p(k)/p_0)\sec\alpha]^{1/2} \quad (4.8)$$

where  $\tau$  is the transmitted part of the scattered radiation and  $p(k)$  is the pressure at level  $k$ ,  $p_0 = 1000$  mb.

Transmission functions for different cloud types are taken from Grandin (1983):

$$\begin{aligned} \zeta_1 &= 0.90 - 0.040 \sec\alpha \text{ (high clouds)} \\ \zeta_2 &= 0.45 - 0.010 \sec\alpha \text{ (medium clouds)} \\ \zeta_3 &= 0.35 - 0.015 \sec\alpha \text{ (low clouds)} \\ \zeta_4 &= 0.16 + 0.005 \sec\alpha \text{ (surface clouds, i.e. fog)} \end{aligned} \quad (4.9)$$

When no clouds are present, the solar radiation flux density at level  $k$  is:

$$\Phi^S(k) = \Phi^S(0)(\tau(k) - A_w(k))\cos\alpha, \quad (4.10)$$

where  $\Phi^S(0)$  is the solar constant ( $= 1395 \text{ Wm}^{-2}$ ). Due to clouds, the solar radiation is further attenuated according to the formula

$$\Phi_C^S(k) = \Phi^S(k)P(k) \quad (4.11)$$

where  $P(k)$  is the reduction factor due to clouds

$$P(k) = \prod_{n=1}^{N(k)} [1 - c_n (1 - \zeta_n)],$$

where  $c_n$  is the coverage of high, medium, low and boundary layer clouds. The cloudiness is separated into these four categories by defining high ( $p < 0.6p_s$ ), medium ( $0.6p_s < p < 0.8p_s$ ), low ( $0.8p_s < p < 0.99p_s$ ), and boundary layer clouds ( $0.99p_s < p < p_s$ ). The levels of separation correspond to values of the vertical index  $k_1$ ,  $k_2$ , and  $k_3$ . Hence,

$$c_n = \max \{a_k\}_{k=k_{n-1}^{n-1}}^{k=k_n^{n-1}},$$

and  $N(k) = n$  if  $k \in \{k_{n-1}, \dots, k_n - 1\}$  where  $k_0 = 1$ . Figure 4.3 illustrates the principle.

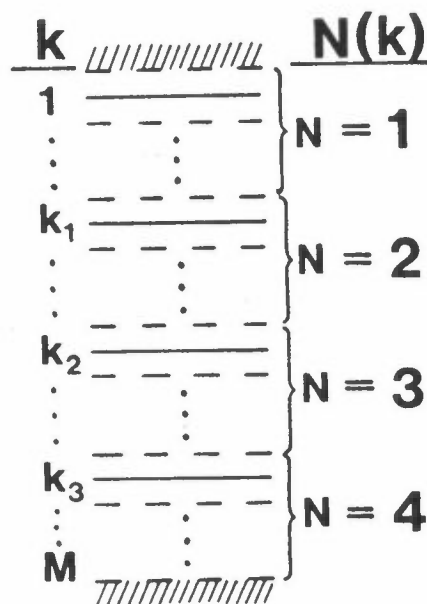


Figure 4.3: Sketch of how the model atmosphere is separated into four main cloud layers in the solar radiation calculations.

The amount of solar radiation reaching the ground level and used in the ground surface temperature equation is then:

$$\Phi_s^S = \begin{cases} \Phi^S(0)(1-A)P(M+1)(\tau(M+1)-A_w(M+1))(\vec{n} \cdot \vec{n}_s), & \text{for } \vec{n} \cdot \vec{n}_s > 0 \text{ and } \cos \alpha > 0. \\ 0, & \text{for } \vec{n} \cdot \vec{n}_s \leq 0 \text{ or } \cos \alpha \leq 0 \end{cases} \quad (4.12)$$

where  $A$  is the albedo of the ground,  $\vec{n}$  is a unit vector pointing towards the sun and  $\vec{n}_s$  is the unit normal vector for the ground surface. Heating of the atmosphere due to solar radiation is neglected.

The zenith angle for the sun is given by  $\alpha$  in the equation

$$\cos \alpha = \sin \delta \sin \beta + \cos \delta \cos \beta \cos t_h,$$

where  $\delta$  is the sun's declination given in degrees by the formula

$$\delta = 23.5 \sin \frac{2\pi}{360} [D - D_0].$$

$\beta$  is latitude,  $t_h$  is local time hour angle,  $D$  is the day no. of the year and  $D_0$  is the day no. of the spring equinox ( $D_0 = 80$ ). The local time hour angle is given in degrees by  $t_h = (t_{GMT} - t_{GMT,N}) \cdot 15 + \lambda$  where  $t_{GMT}$  and  $t_{GMT,N}$  is GMT-time at present and at noon, and  $\lambda$  is the longitude. When the ground surface is flat, then  $\vec{n} \cdot \vec{n}_s = \cos \alpha$ . If one wish to take into account the slope the earth's surface, then

$$\vec{n} \cdot \vec{n}_s = (-(\partial z_s / \partial x) n_x - (\partial z_s / \partial y) n_y + n_z) / (1 + (\partial z_s / \partial x)^2 + (\partial z_s / \partial y)^2)^{1/2} \quad (4.13)$$

where

$$\vec{n} = \begin{bmatrix} n_x \\ n_y \\ n_z \end{bmatrix} = \begin{bmatrix} -\cos \beta \cos \delta \sin t_h - \sin \gamma \sin \beta \cos \delta \cos t_h - \sin \gamma \cos \beta \sin \delta \\ \sin \gamma \cos \delta \sin t_h - \cos \delta \sin \beta \cos \delta t_h + \cos \gamma \cos \beta \sin \delta \\ \cos \alpha \end{bmatrix} \quad (4.14)$$

Here,  $\gamma$  is the angle between local north and the  $y$ -direction in the cartesian grid.

#### 4.4 GROUND/SEA SURFACE EQUATIONS

The variations in albedo, roughness parameter, heat capacity, and thermal conductivity due to the horizontal distribution of land, sea, snowcover and forrests, are prescribed. Over sea, the surface temperature is prescribed, and the surface air is assumed to be saturated with respect to water

Over land a ground surface temperature equation is solved. It may optionally be solved as a prognostic equation or as a diagnostic equation assuming a vanishing net flux density (Newton/Raphson solution method). The latter approach can be used if a surface temperature is missing at the start of an integration. The equation takes into account the flux density of latent and sensible heat, long and short wave radiation and heat conduction into the ground (Deardorff, 1978).

The equation is

$$C_S \frac{\partial T_S}{\partial t} = \Phi_S^L + \Phi_S^S + H_S^T + L R_S^T + H^C - B_S \quad (4.15)$$

where

$C_S$  = ground surface heat capacity per unit area.

$\Phi_L^S$  = short wave radiation flux density (positive downwards).

$\Phi_S^L$  = long wave radiation flux density (positive downwards).

$H_S^T$  = downward flux density of sensible heat due to turbulence

$$= \rho_S \Pi_S u_* \theta_*.$$

$R_S^T$  = downward flux density of moisture due to turbulence

$$= \rho_S u_* q_*.$$

$L$  = heat of vaporization

$H^C$  = heat conduction from the deep soil

$B_S$  = black body radiation flux density from ground

If the heat flux towards the surface from above varies periodically with time, and the surface temperature in response varies as:

$$T_s = T_0 + \Delta T_s \sin\left(\frac{2\pi t}{P}\right)$$

where  $P$  is the period,  $\Delta T_s$  is the amplitude and  $T_0$  a constant mean, then the temperature at a depth  $\Delta z$  below the surface will vary as:

$$T = T_0 + \Delta T_s \exp\left(-\frac{2\pi\Delta z}{\delta}\right) \sin\left(2\pi\left(\frac{t}{P} - \frac{\Delta z}{\delta}\right)\right)$$

(Eliassen and Pedersen, 1977). If the thermal conductivity is  $\zeta$ , the soil specific heat  $c$ , and soil density  $\rho$ , then

$$\delta = 2 \left(\pi \frac{\zeta P}{c\rho}\right)^{1/2}$$

Eliassen and Pedersen gives the properties  $\delta$ ,  $c$ ,  $\rho$  and  $\zeta$  for different soil types and periods  $P$ .  $\delta/2$  may be taken as the depth of which the wave with period  $P$  penetrates, and can be approximated by 0.40 m for the daily wave ( $P = 86400$  s) independently of soil type.  $H^C$  is then parameterized by

$$H^C = \frac{2\zeta}{\delta} (T_d - T_s) \quad (4.16)$$

We have chosen  $C_s = 0.7 \cdot 10^6$  J/m<sup>2</sup>K and  $2\zeta/\delta = 2.58$  W/m<sup>2</sup>K for bare ground and  $C_s = 0.5 \cdot 10^6$  J/m<sup>2</sup>K and  $2\zeta/\delta = 1.84$  W/m<sup>2</sup>K for snow covered ground. The albedo  $A$  is 0.30 for bare ground and 0.5 for snow. The deep soil temperature  $T_d$  is 273.15 K for snow covered ground and 288 K for bare ground (summer value). The "snow values" reflects that there always will be a layer of vegetation, changing the parameters from that of a purely snowcovered plain.

If a surface temperature is missing in the start of an integration, the ground surface temperature can be found by solving a diagnostic equation for  $T_s$  by assuming a balance between the heat fluxes at the earth's surface. A Newton/Raphson iteration technique is then used:

$$T_s^{\mu+1} = T_s^{\mu} - H_a(T_s^{\mu})/H'_a(T_s^{\mu})$$

where  $H_a$  is the right hand-side of eq. (4.15) and  $H'_a$  is the equation obtained by differentiation with respect to  $T_s$ :

$$H'_a(T_s) = \frac{\partial}{\partial T_s} (H_s) + L \frac{\partial}{\partial T_s} (R_s) - \frac{2\zeta}{\delta} 4\sigma T_s^3$$

Here  $\sigma$  is Stefan-Boltzmann's constant ( $= 6.5669 \cdot 10^{-8} \text{ W/m}^2 \text{ K}^4$ ).

The surface flux density of moisture is proportional to  $(q_g - q_{\text{air}})$  where  $q_g$  is the specific humidity in the air very close to the ground and  $q_{\text{air}}$  is the g specific humidity in the atmospheric surface layer. It is convenient to replace this relation by a relation dependant on surface temperature. By definition of  $\alpha$ :

$$q_g - q_{\text{air}} \stackrel{\text{def}}{=} \alpha (q_{\text{sat}}(p_s, T_s) - q_{\text{air}}) \quad (4.17)$$

which implies

$$q_g = \alpha q_{\text{sat}}(p_s, T_s) + (1-\alpha) q_{\text{air}}$$

The coefficient  $\alpha$  is related to the soil moisture  $W$  (depth of extracted liquid water),  $\alpha = \min(W/W_k, 1)$  where  $W_k$  is the maximum value of  $W$  with no runoff. An obvious restriction is that  $q_g \leq q_{\text{sat}}(T_s)$ . Deardorff (1978) discusses different methods to calculate  $\alpha$ . We have chosen to prescribe it and keep this prescribed value constant in our experiments.

#### 4.5 CONDENSATION AND PRECIPITATION

The scheme is diagnostic. The model equations are first integrated without condensation processes included, and the effects of condensation are added in a second step. The scheme is initiated if supersaturation is found in a grid point. As the horizontal resolution increases, the grid scale dynamics can be assumed to deal with the mesoscale organization of cloud cells into clusters, squall lines etc. Therefore, the parameterization only takes into account individual cloud cells, and no relation between convection and large scale convergence of moisture is explicitly assumed.



a. Supersaturation within an absolutely stable stratification

Any excess moisture is condensed with the latent heat warming the air. The implicit equations to be solved are:

$$q_v + \Delta q_v = q_{\text{sat}}(T+\Delta T)$$

$$c_p \Delta T + L \Delta q_v = 0$$

$$\Delta q_v + \Delta q_w = 0$$

where  $q_{\text{sat}}(T)$  is the saturation humidity at temperature  $T$  (and pressure  $p$ ),  $q_v$  is water vapour to be adjusted ( $\Delta q_v$ ), and  $\Delta q_w$  is condensed liquid water by the process. By approximating  $q_{\text{sat}}(T+\Delta T)$  by a first order Taylor expansion and utilizing Clausius-Clapeyron's equation for the derivative of  $q_{\text{sat}}$  with respect to temperature, we get:

$$\Delta q_v = (q_{\text{sat}}(T) - q_v) / \left(1 + \frac{\epsilon L^2 q_{\text{sat}}(T)}{C_p R T^2}\right), \quad \Delta T = -\frac{L}{c_p} \Delta q_v', \quad \text{and} \quad \Delta q_w = -\Delta q_v.$$

$$\text{Hence, } \left. \begin{aligned} (\theta_t)_{\text{lat}} &= (c_p/\Pi) (\Delta T/\Delta t) \\ (q_t)_{\text{phase}} &= \Delta q_v/\Delta t \end{aligned} \right\} \quad (4.18)$$

The time required for the adjustment to take place, is  $\Delta t$ . When water vapour is condensed ( $\Delta q_v < 0$ ), an increase in temperature through release of latent heat ( $\Delta T > 0$ ) and an increase in cloud liquid water ( $\Delta q_w > 0$ ) is caused.

b. Supersaturation within a conditionally stable stratification

In this case, a Kuo-like scheme (Kuo, 1965) distributes heat and moisture within the unstable atmosphere. A "cloud" is defined by following a moist adiabat from the saturated level until it intersects the given sounding. We want to distribute the moisture and heating within this part of the model atmosphere, so that some part of the grid square contains a cloudy air with temperature and humidity taken from the moist adiabatic values, while the remaining parts are cloudfree (environmental) air.

If (a) is the fraction of the grid covered by clouds, and we assume that the integrated enthalpy is conserved, then:

$$\int_{\text{cloud}} a(c_p T_c + Lq_{vc}) dp + \int_{\text{cloud}} (1-a)(c_p T_e + Lq_{ve}) dp = \int_{\text{cloud}} (c_p T + Lq_v) dp$$

where  $(T_c, q_{vc})$  are cloud values,  $(T_e, q_{ve})$  are environmental values, and  $(T, q_v)$  are given values to be adjusted. By assuming that (a) is a constant one obtains:

$$a = \frac{\int (q_v - q_{ve} + \frac{c_p}{L} (T - T_e)) dp}{\int (q_{vc} - q_{ve} + \frac{c_p}{L} (T_c - T_e)) dp}$$

The temperature and humidity of the environment have to be estimated. Here, the same assumption as in the Kuo-scheme (Kuo, 1965 - 1974) is used. As soon as the cloud is developed and the latent heat is released, it is dissolved by mixing with the environmental air. We therefore put  $T_e = T$ . We will further assume that this is also the case for the humidity. This leads to:

$$a = \frac{\int (q_v - q_{ve}) dp}{\int (q_{vc} - q_{ve} + \frac{c_p}{L} (T_c - T)) dp}, \quad q_{ve} = \min(q_v, q_{\text{sat}}(T))$$

The denominator is the amount of water vapor needed over the unstable column to obtain a cloud filling the whole grid space, while the numerator is the actual surplus of water vapor at present.

The mean temperature and specific humidity after cloud production is:

$$T' = a T_c + (1-a) T$$

$$q'_v = a q_{vc} + (1-a) q_{ve}$$

so that  $\Delta T = a(T_c - T)$  and  $\Delta q_v = a(q_{vc} - q_{ve})$ . Finally,

$$(\theta_t)_{\text{lat}} = (c_p/\Pi) (\Delta T/\Delta t)$$

$$(q_t)_{\text{phase}} = \Delta q_v/\Delta t \tag{4.19}$$

In the real atmosphere the temperature is increased by latent heat release and convective transport of sensible heat. In the scheme, the latter is not estimated and it is assumed that the temperature is increased due to latent heat release only. The condensed liquid water is then:

$$\Delta q_w = c_p \Delta T/L = a c_p (T_c - T)/L$$

c. Unstable stratification with saturated air aloft

If (a) becomes greater than one, which may happen for a large surplus of moisture in a level and/or a nearly moist adiabatic stratification above, its value can no longer be regarded as the fractional cloud cover. A scheme of the moist adiabatic adjustment type (Manabe et al., 1965) could be used to distribute the latent heat of condensation over the unstable layers in such a way that the final lapse rate becomes moist neutral.

To calculate the moist adiabat that the atmosphere finally adjusts to, an approach which avoids iterations is chosen. Firstly, the scheme already described is used with (a) = 1, adjusting the model atmosphere to be exactly moist adiabatic. Secondly, the extra moisture

$$\Delta Q = (a-1) \int [q_{vc} - q_{ve} + \frac{c_p}{L} (T_c - T)] \frac{dp}{g},$$

is distributed within the cloud according to

$$\int (\delta q_v + \frac{c_p}{L} \delta T) \frac{dp}{g} = \Delta Q, \quad (4.20)$$

where  $\delta q$  and  $\delta T$  are further changes in humidity and moisture. Since both the final lapse rate and the preliminary adjusted lapse rate are moist adiabates, we have

$$\delta q_v = q_{sat}(T_c + \delta T) - q_{sat}(T_c)$$

or approximately

$$\delta q_v = \frac{\epsilon L q_{sat}(T_c)}{RT_c^2} \delta T \quad (4.21)$$

Since  $\delta T = T' - T_c$  where both  $T'$  and  $T_c$  are moist adiabats, the derivative of  $\delta T$  with respect to pressure is

$$\frac{\partial}{\partial p} (\delta T) = \frac{\partial}{\partial p} (T' - T_c) = \frac{RT'}{c_p p} \zeta' - \frac{RT_c}{c_p p} \zeta_c$$

where

$$\zeta(T) = \frac{1 + \frac{L}{RT} q_{\text{sat}}(T)}{1 + \frac{\epsilon L^2}{c_p RT^2} q_{\text{sat}}(T)}$$

Here,  $\zeta(T)$  is the deviation of the moist adiabatic lapse rate from that of a dry adiabat (Eliassen and Pedersen, 1977). By writing  $\zeta(T') = \zeta(T_c) + (\partial\zeta/\partial T) \cdot \delta T$ , performing the derivation  $\partial\zeta/\partial T$  and omitting second order terms, one ends up with

$$(\delta T)_p = \gamma \delta T$$

where

$$\gamma = \frac{RT_c}{c_p p} \frac{\frac{\epsilon L^2 q_{\text{sat}}(T_c)}{R^2 T_c^3} (1 - \zeta_c \frac{\epsilon L}{p T_c})}{1 + \frac{\epsilon L^2 q_{\text{sat}}(T_c)}{c_p RT_c^2}}$$

Then by integration, one gets:

$$\delta T(p) = \delta T(p_b) \exp\left(-\int_p^{p_b} \gamma dp\right) \quad (4.22)$$

where  $p_b$  is the pressure at cloud base and  $p$  is the pressure within the cloud. Insertions of (4.22) and (4.21) into (4.20) give:

$$\delta T(p_b) = \frac{\Delta Q}{\int_{\text{cloud}} \left[ \frac{c_p}{L} + \frac{\epsilon L q_{\text{sat}}(T_c)}{RT_c^2} \right] \exp\left(-\int_p^{p_b} \gamma dp\right) \frac{dp}{g}}$$

while  $\delta T(p)$  at other levels within the cloud is found from (4.22).

Total changes in temperature and moisture are then;

$$\begin{aligned}\Delta T &= T_c - T + \delta T \\ \Delta q_v &= q_{vc} - q_{ve} + \left( \frac{\epsilon L q_{sat}(T_c)}{RT_c^2} \right) \delta T, \text{ and} \\ \Delta q_w &= c_p \Delta T/L, \text{ and thus} \\ (e_t)_{lat} &= (c_p/\Pi)(\Delta T/\Delta t) \\ (q_t)_{phase} &= \Delta q_v/\Delta t\end{aligned}\tag{4.23}$$

By this method a sub-grid convective cloud is produced if the moisture is less than what is needed to saturate the whole grid volume. If sufficient moisture are at hand, a stratiform cloud, possibly extending over several model layers with a moist adiabatic stratification is produced.

The test for supersaturation is then performed for the model layer just above the cloud top until all layers have been checked for supersaturation. Thus stratiform and convective clouds (as defined by this scheme) may exist on the top of each other.

The total amount of condensed water is removed through precipitation;

$$\begin{aligned}P &= \int_{0q}^1 \Delta q_w \frac{p^* d\sigma}{g}. \text{ Numerically one gets} \\ P &= \sum_{k=1}^M (\Delta q_w)_k p_k^* \Delta \sigma_k / g\end{aligned}\tag{4.24}$$

## 5 LATERAL BOUNDARY CONDITIONS

The use of a limited area, nested grid technique is necessary due to limitations of capacity on electronic computers both with regard to core storage and computational speed. For a proper description of a phenomenon, one should employ a grid with adequate space resolution, and simultaneously cover an area large enough to contain the region of influence. Unfortunately, it is not possible in practice to study mesoscale structures with the required accuracy by the use of e.g. a hemispheric model with uniform grid resolution. Therefore the idea of combining grids of different sizes (grid nesting) has developed.

The method of nesting can be performed in two different ways. When applying two way interaction, the model equations are solved on a grid with variable density of gridpoints. Hence the finemesh area forecasts affects the coarse mesh forecasts and vice versa. This technique was early applied by Birchfield (1960) in a balanced barotropic model, later by Koss (1971), Ookochi (1972) and Phillips and Shukla (1973) in baroclinic primitive equation models. When applying one-way influence, the coarse mesh computations influence the fine mesh forecasts, but not vice versa. This method has the preference that the fine mesh integration can be carried out subsequent to the coarse mesh model. Therefore, this is a powerful tool for regional weather forecast centra that receive forecasts from a global centre. However, one has to face the problem of boundary conditions on the intersection between the coarse and fine mesh grid. In primitive equation models one has to pay special attention to the gravity mode that should not be reflected at the boundary. For filtered models only the Rossby mode is present and the problem is simpler. The boundary conditions for limited area quasi-geostrophic models were discussed already in the pioneering paper by Charney et al. (1950). They stated that both components of the flow (tangential and normal to the boundary) should be prescribed at an instream boundary, while only one component should be prescribed at an outstream boundary. The second component of the flow at the outstream boundary should be computed from the interior data.

The first experiments with the one-way nesting method were presented by Hill (1968). He prescribed both components of the flow at all parts of the boundary, and thus had to control the spurious oscillations at outstream regions by artificial smoothing. He integrated a baroclinic quasi-geostrophic model, while Wang and Halpern (1970) integrated the shallow water equations with the same overspecified boundary condition. Shapiro and O'Brien (1970) integrated the very simple non-divergent barotropic model. They employed the boundary condition suggested by Charney et al. (1950), applying a pseudo-Lagrangian scheme at the outstream boundaries. This approach did not lead to spurious waves. Later, a number of extrapolation methods at outstream boundaries has been proposed. Other methods suggest overspecified boundary conditions together with artificial smoothing techniques. A review was given by Miyakoda and Rosati (1977). Most of the charac-

teristic problems connected with limited area models, are briefly reviewed by Sundstrøm and Elvius (1979), and Davies (1983).

The flow relaxation scheme (Davies 1976, Kållberg and Gibson, 1977) forces the prognostic variables to relax towards the external specified fields in a marginal zone near the boundaries. This method is used for the fine mesh model described in this report. The method implies overspecified boundary fields according to the rules obtained from the theory of boundary conditions for initial-boundary value problems (e.g. Courant and Hilbert, 1962, Ch. VI). However, as demonstrated by Anthes and Warner (1978), overspecified boundary conditions should be applied to mesoscale models, in order to avoid spurious mass loss and accelerations within the limited area of integration. Near the boundaries, some damping methods must then be applied to remove spurious waves. When using the relaxation method, such a damping is included implicitly (Newton-damping) and no additional operations are necessary.

Even though the flow relaxation scheme solves most of the boundary problems associated with limited area models, it creates some new. If the model providing boundary data has different physical forcing than the limited area model, noise may develop within the relaxation zone close to the boundary. In experiments with a mesoscale model with a comprehensive physical forcing, we found that a frontal zone developed within the relaxation zone and eventually influenced the whole integration area. The problem was remarked by Anthes and Warner (1978), who suggested that the tendencies due to vertical heat flux should be added to the otherwise specified temperature on the boundary. The boundary values would then be more compatible with the solutions in the interior. However, Anthes and Warner did not employ the relaxation technique.

An ideal open boundary treatment should be able to leave meteorological modes undisturbed both at inflow and outflow boundaries, completely transmit gravity waves out of the integration area, and allow physical forcing in the model atmosphere without spurious effects being created near the boundaries. The relaxation technique of Davies (1976) and Kållberg and Gibson (1977) has shown to satisfy the first two of these criteria. In this chapter we will show how the

relaxation method can be extended to take care of different physical forcing.

### 5.1 THE RELAXATION SCHEME

The practical application of the relaxation technique is first to perform the time integration on the inner area, and then each timestep relax the solution towards the external fields in the relaxation zone.

Applied on the equation

$$\frac{\partial X}{\partial t} + F(X) = 0$$

where  $X$  is a prognostic model variable, the Leapfrog scheme give

$$\tilde{X}^{n+1} = X^{n-1} - 2\Delta t F(X^n)$$

The preliminary value,  $\tilde{X}^{n+1}$  is then adjusted towards the external solution by

$$X^{n+1} = \alpha \hat{X}^{n+1} + (1-\alpha) \tilde{X}^{n+1} \quad (5.1)$$

where  $\hat{X}^{n+1}$  is the external specified field at time  $(n+1)$ . The relaxation parameter  $\alpha$  varies smoothly between 1 at the boundary and 0 inside the relaxation zone. Several functional forms are possible. We have chosen  $\alpha = [(N-n)/N]^2$ , where  $N$  is the width of the relaxation zone measured in grid lengths, and  $n$  is the distance in grid units from the boundary  $n \in (0, N)$ . For  $N=6$ , we have  $\alpha \in \{1.00, 0.69, 0.44, 0.25, 0.11, 0.03\}$ .

If  $\hat{X}$  does not carry information about mesoscale physical forcing, it is clear that strong gradients in  $X$  may occur within the relaxation zone. The problem may be solved by integrating the external fields due to the physical forcing on the inner area.

We put  $F(X) = F_a(X) + F_p(X)$



where  $F_p(X)$  is due to physical forcing alone, and  $F_a(X)$  is the residue:  $F_a(X) = F(X) - F_p(X)$ . Then,

$$X_p^{n+1} = X_p^{n-1} - 2\Delta t F_p(X^n) \quad (\text{integrate due to physics alone})$$

$$\tilde{X}^{n+1} = X^{n-1} - 2\Delta t F(X^n) \quad (\text{preliminary integration}) \quad (5.2)$$

$$X^{n+1} = \alpha(\tilde{X}^{n+1} + X_p^{n+1}) + (1-\alpha)\tilde{X}^{n+1} \quad (\text{adjust towards boundary fields})$$

Since the computation of the physical forcing is confined to a vertical column, the computation may be performed for the whole integration area. The boundary values will then be consistent with the inner area values.

## 5.2 EXPERIMENTS ON BOUNDARY CONDITIONS

The successful behaviour of the scheme can be demonstrated by a series of integrations with simple numerical models. The simplest model describing propagation of disturbances is the one-dimensional advection equation,

$$C_t = -UC_x$$

In the first experiment with this model, an initial disturbance

$$C_0 = \Delta H \left( e^{-\left(\frac{X-X_m}{X_0}\right)^2} - e^{-4} \right),$$

is imposed in the middle of an integration area consisting of 33 gridpoints. Here  $X_m$  is the mid point of the integration area,  $X_0$  is 5 gridlengths,  $\Delta H = 100\text{m}$  and  $C_0$  is restricted to be positive. The grid distance is 10 km, the advection speed  $U$  is  $10\text{ms}^{-1}$ , and the time step used is 450 s. The equation is solved by centered differences in space and by use of the Leapfrog scheme in time. The width of the relaxation zone is chosen to be 6 gridlengths for all the experiments presented in this subsection. At the boundary the external solution  $C_R = 0$  is imposed. As seen from Fig. 5.1a the

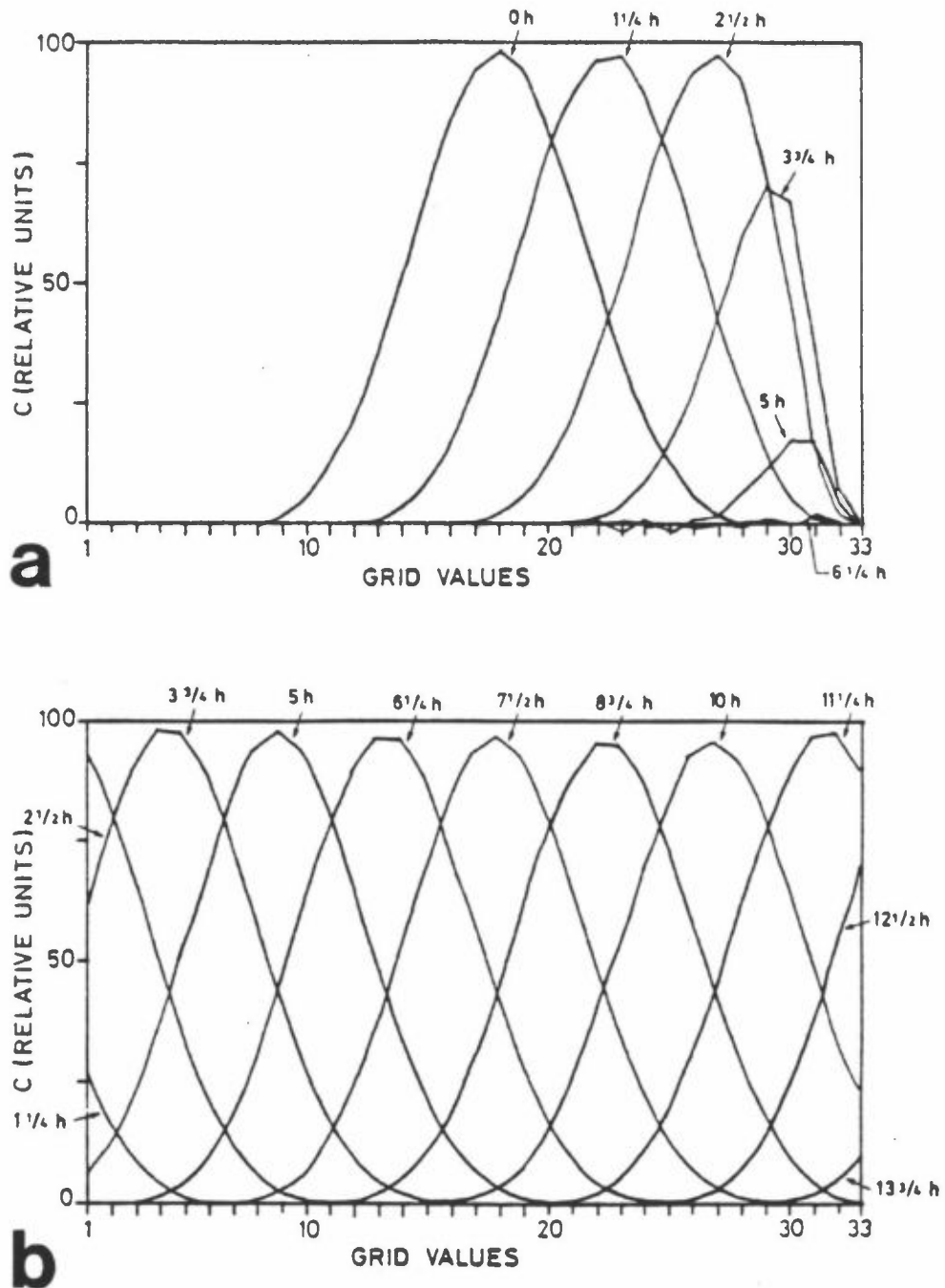


Figure 5.1: Results from tests with boundary relaxation scheme on advection, showing amplitudes of disturbance at different times during integration.

a) No information in boundary fields.

b) Boundary fields are the analytical solution to the advection equation.

initial disturbance propagates towards the boundary with no change of amplitude until it reaches the relaxation zone. Then the amplitude is reduced and the disturbance leaves the integration area with negligible spurious energy created.

When a time-dependent solution is imposed at the boundary (i.e. the disturbance approach the integration area from outside) the disturbance is almost perfectly transmitted through the integration area (Fig. 5.1b). Here the specified field is the analytical solution of the advection equation.

The one-dimensional advection equation has only one degree of freedom. A more complicated system is the one dimensional shallow water equations which describe two gravity modes and a Rossby-mode.

The equations read:

$$u_t = fv - uu_x - \varphi_x$$

$$v_t = -fu - uv_x + fu_g$$

$$\varphi_t = -u\varphi_x - \varphi u_x$$

Here,  $\varphi$  is the geopotential  $\varphi = gz$ , where  $z$  is the height,  $(u,v)$  is the wind velocity,  $f$  is the Coriolis parameter and  $u_g$  is the geostrophic wind in the  $x$ -direction. In the experiment we put  $u_g = 0$  and initiate the problem by assuming  $u = v = 0$ ,  $\varphi = \varphi_0$  initially. The external fields are chosen to  $\hat{u} = \hat{v} = 0$ ,  $\hat{\varphi} = gH$ . This is an unbalanced state which generates gravity waves propagating away from the initial disturbance and initiates a geostrophic adjustment process. The equations are solved in a domain containing 32 grid points by using centered finite differences in space and the Leapfrog scheme in time. No diffusion or smoothing is used. The initial condition  $\varphi_0$  is chosen as

$$\varphi_0 = [H + \Delta H(e^{-\frac{x-x_m}{x_0}} - e^{-4})]g$$

where  $\Delta H = \sqrt{e/2} u_g f x_o / g$  gives a maximum geostrophic wind of  $u_g = 2 \text{ ms}^{-1}$ ,  $x_m$  is the central point of the integration area,  $x_o = 5d$ , and  $f = 1.26 \cdot 10^{-4} \text{ s}^{-1}$  ( $60^\circ \text{ N}$ ).

In the first experiment the grid distance is 10 km and the scale height is  $H = 1 \text{ km}$ . The Rossby radius of deformation  $L_R = \frac{\sqrt{gH}}{f} = 1000 \text{ km}$ . The scale of the initial disturbance is clearly less than this and the final state is determined by the initial wind (which is zero). One would expect gravity waves leaving the initial disturbance in both directions. Fig. 5.2a shows that this actually happens. The gravity waves neatly leave the integration area. Only some negligible noise is created (grid length twice the grid-distance) and the relaxation technique works satisfactory.

In a second experiment the grid distance is chosen to 100 km. The other parameters are unchanged. Gravity waves still leave the initial disturbance, but the scale of the disturbance is so large that some of the wind adjusts towards the massfield. As seen from Fig. 5.2b the gravity waves leave the integration area while wind and geopotential gradually adjust to a geostrophic balance. This result shows that the relaxation technique separates the different modes of the solution in a proper way. The gravity waves disappear while the Rossby mode is retained more or less unaffected.

A harder test of the boundary scheme, is to impose a completely different physical forcing on the interior integration area than on the exterior from which the boundary fields are taken. A two-dimensional primitive equation model in  $\sigma$ -coordinates ( $\sigma = (p - p_T) / (p_S - p_T)$ ) was constructed to demonstrate this effect. The sea-breeze dynamics are driven by physical forcing through differential heating due to contrasts between land and sea.

The basic state is a calm atmosphere in hydrostatic equilibrium ( $u = v = \dot{\sigma} = \nabla\phi = \nabla e = \nabla p_S = 0$ ,  $\frac{\partial e}{\partial \sigma} = \gamma$ , where  $\gamma$  corresponds to a lapse rate of  $\frac{\partial T}{\partial z} = 0.6 \frac{\text{K}}{100 \text{ m}}$ ). The equations describing deviations from this state read:

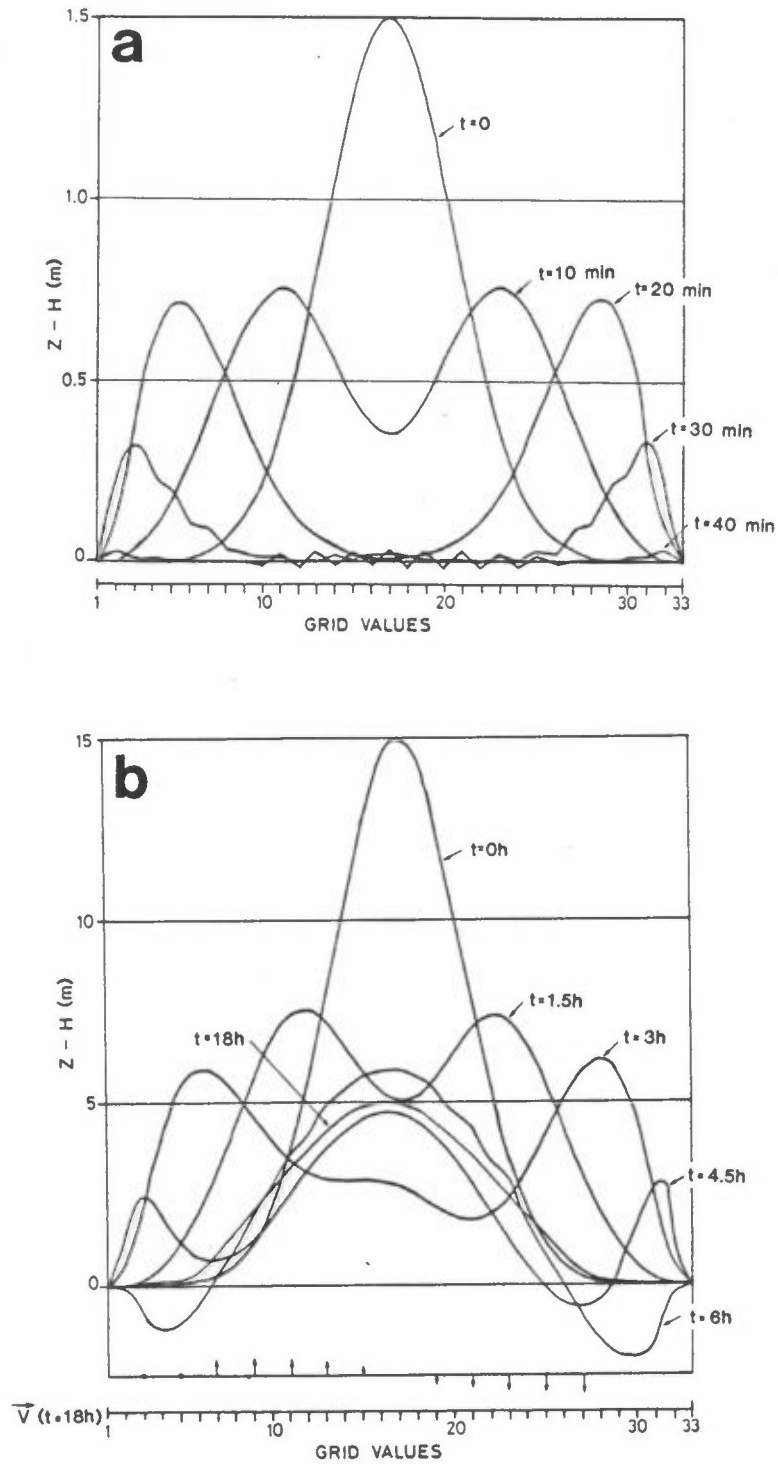


Figure 5.2: Results from tests with boundary relaxation scheme on gravity waves showing deviations from initial disturbance (m) at different times during integration. The Rossby radius of deformation is 1000 km.

a) Small scaled, initial imbalance. The length scale is 150 km.

b) Large scaled, initial imbalance. The length scale is 1500 km.

$$\begin{aligned}
u_t + uu_x + \dot{\sigma}u_\sigma &= fv - \varphi_x - e\pi_x & (a) \\
v_t + uv_x + \dot{\sigma}v_\sigma &= -fu & (b) \\
e_t + ue_x + \dot{\sigma}(e_\sigma + \gamma) &= (e_t)_{\text{phys}} & (c) \\
\varphi_\sigma + e\pi_\sigma &= 0 & (d) \\
(p_S)_t + (p_*u)_x + (\dot{\sigma}p_*)_\sigma &= 0 & (e)
\end{aligned} \tag{5.3}$$

$$p_* = p_S - p_T + p_O, \quad p_O = 1000 \text{ mb}, \quad \pi = c_p \left(\frac{p}{p_O}\right)^{R/c_p}$$

The equations are solved in a two-layer model and on a domain containing 32 grid-points along the x-direction. We assume that  $\dot{\sigma} = 0$  at  $p = p_T = 850$  mb. The model layers are given by  $\sigma = (0.0, 0.5, 1.0)$ .  $\dot{\sigma}$  and  $\varphi$  are given at intersections between layers ( $\sigma = 0.0, 0.5, 1.0$ ) while  $u, v, e$  are given in the middle of layers ( $\sigma = 0.25, 0.75$ ).

The geopotential is found by integrating the hydrostatic equation (5.3d) from ground where  $\varphi = 0$ . The vertical velocity and the surface pressure tendency are found from the continuity equation (5.3e) by integration from the model top. Time derivatives of  $u, v$  and  $e$  are achieved from (5.3 abc). The Leapfrog-scheme is used for time integration, and space derivatives are determined by centered finite differences. The grid-distance is 10 km and the Coriolis parameter  $f = 10^{-4} \text{ s}^{-1}$ . The chosen physical forcing is  $(e_t)_{\text{phys}} = 10^{-4} \text{ K/s}$  (corresponds to about 8.5 K heating per day at 1000 hPa). The forcing is imposed only over the right half of the integration area and in the lowest model layer to simulate land/sea differences in physical forcing. In the relaxation zone the solution is adjusted towards a specified solution, which in this experiment is chosen to be the same as the basic state. The model is run both with boundary scheme (5.1) and (5.2).

Simulations with and without the extended version of the boundary relaxation scheme are shown in Figs 5.3 and 5.4. Figs. 5.3 show the evolution of the surface pressure together with winds in the two layers after 5 hours of integration for runs without and with the extended boundary relaxation scheme respectively.

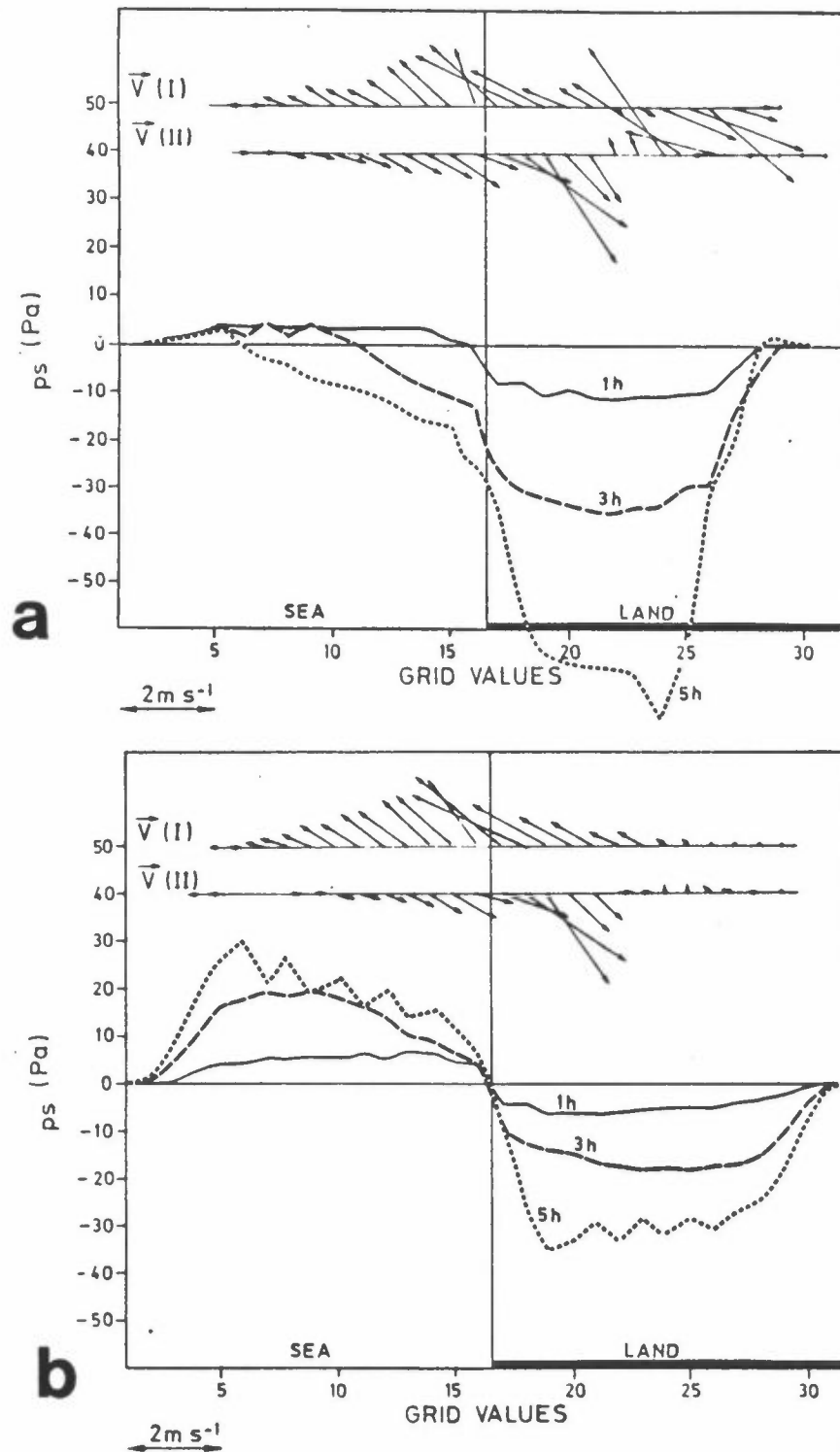


Figure 5.3: Results from tests with boundary relaxation scheme. Arrows are winds at level I and II after 3 h of integration. The curves show deviation in surface pressure ( $p_s$ ) from the initial state, after 1, 3 and 5 h of integration.  
 a) Original version of boundary scheme.  
 b) Extended version of boundary scheme.

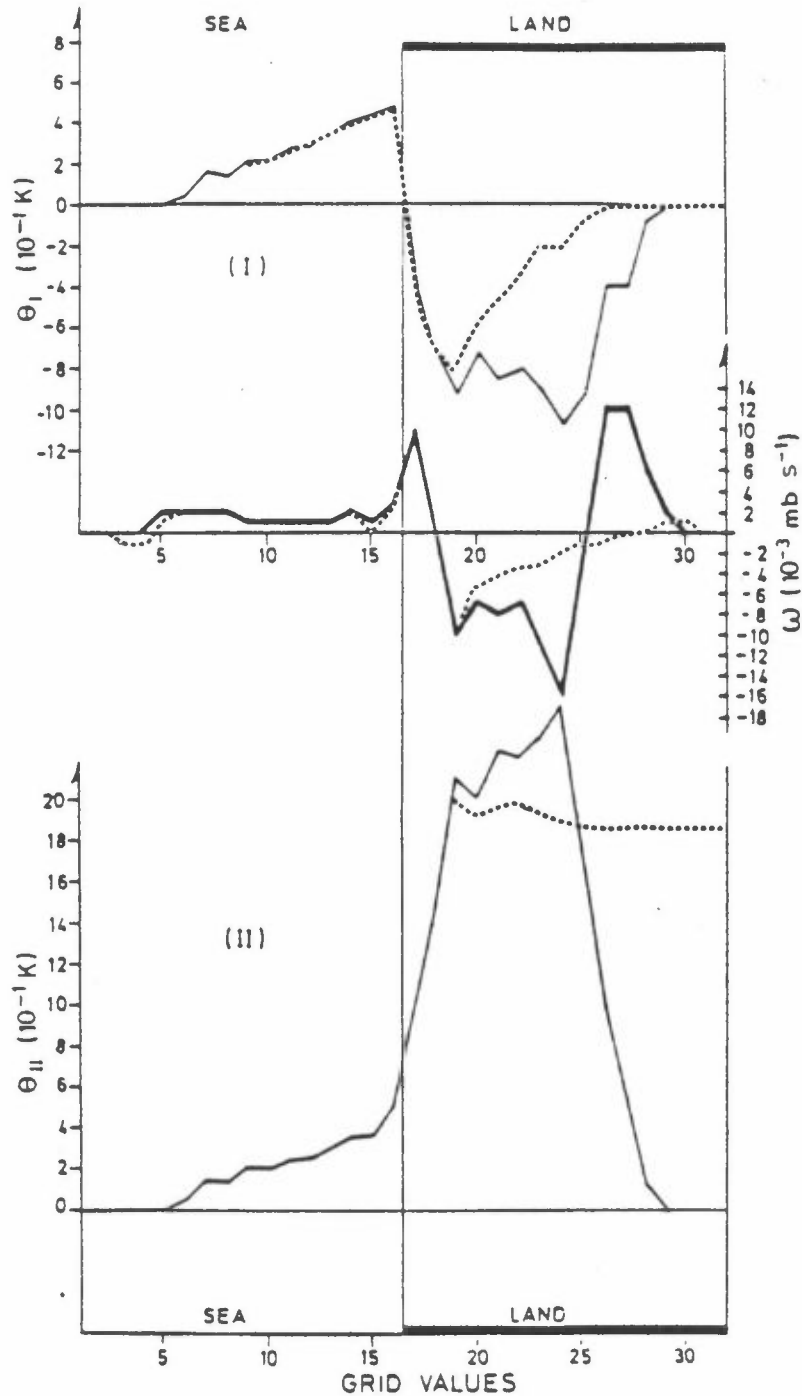


Figure 5.4: Results from tests with boundary relaxation scheme and physical forcing. I and II refer to upper and lower level in the two level model respectively. Continuous lines are results after 3 h with the original boundary scheme, while dotted lines shows results after 3 h with the new scheme. The upper and lower curves show deviations in potential temperature ( $\theta$ ) from the initial state (ordinate axis on the left). The curves in the middle shows vertical motion ( $\omega = Dp/dt$ ) (ordinate axis on the right).



when differential heating is taken into account explicitly. Strongest evidence of a spurious solution due to the boundary condition appears, in the flow field. Apparently there are small differences in the area of interest (close to the "coast"). The surface front propagates about 40 km inland and the wind turns along the coast, thus achieving a considerable geostrophic component, as one should expect. However, considerable noise develops close to the relaxation zone. This shows up in the horizontal flow field, in the vertical motion, and in the temperature perturbations (Fig. 5.4). These strong undesired winds, and especially the strong vertical motion, may eventually influence the whole integration area in a more complete model due to initiation of precipitation and subsequent release of latent heat.

### 5.3 CONCLUSIVE REMARKS ON BOUNDARY CONDITIONS

We have shown how the popular boundary relaxation scheme of Davies (1976) and Källberg and Gibson (1977) may be extended to take care of situations where physical forcing is important for mesoscale processes, but not taken into account in the externally specified fields to be used at the boundary. Simulations including gravity modes as well as Rossby modes show how the scheme nicely treats the inflow and outflow of information, with only some negligibly small scale noise created. This noise can be further removed with a wider relaxation zone (Davies, 1983). The method is easily incorporated into three-dimensional limited area models, and is used with the mesoscale model described in this report. The method has performed excellently in the experiments referred to in this report.

## 6 POSSIBLE APPLICATIONS

The model documented in this report is aimed at simulating a wide range of dynamical and physical processes in the atmosphere. The scheme for parameterization of vertical turbulent diffusion requires a certain minimum resolution of the atmospheric boundary layer. The model is therefore specially suited to study phenomena closely connected with boundary layer processes. The atmospheric mesoscale includes several types of such phenomena.

It is well known that the quasi-hydrostatic approximation imposes a lower limit for the spatial and temporal scales of the phenomena to be simulated. The approximation is made for economical reasons; the equation for vertical momentum transforms into a diagnostic equation, and vertically propagating acoustic waves are removed, thus allowing longer timesteps. In this section the lower limit of the grid length  $d$  when applying the quasi-hydrostatic approximation, is examined.

## 6.1 ANALYTICAL SOLUTIONS

Firstly, a brief summary of known properties for pure types of motion studied by analytical methods, is given.

### 6.1.1 Free waves

By the study of small perturbations of an atmosphere in a basic state at rest, one may arrive at a dispersion relationship for free, combined acoustic-gravity waves (Eliassen, 1983). The Coriolis force is neglected, and the dependent variables are transformed so that the coefficients vary little with height. The coefficients of the linearized equations are thus

$$C_s^{-2} = \left(\frac{c_p}{c_v} RT\right)^{-1}; \quad N^2 = \frac{g}{\theta} \theta_z \quad \text{and} \quad \beta = \frac{1}{2} \left(\frac{g}{C_s^2} - \frac{N^2}{g}\right).$$

Here  $C_s$  is the speed of pure sound waves and  $N$  is the Väisälä-Brunt frequency of the basic atmosphere. Assuming that these coefficients are constants, trigonometric solutions may be sought

and a dispersion relation arrived at (Eliassen, 1983):

$$\kappa^2 = \omega^2 \left[ \frac{m^2 + \beta^2}{N^2 - a \cdot \omega^2} + \frac{1}{C_s^2} \right] \quad (6.1)$$

where the tracer ( $a$ ) vanishes for the quasi-hydrostatic approximation and equals unity in the non-hydrostatic case. When  $m^2 > 0$  we have internal (or vertically wavelike) waves, while  $m^2 < 0$  corresponds to external waves with exponential dependence with height. In the non-hydrostatic case there are two types of internal waves; one which is dominated by acoustic effects (compressibility) and another dominated by gravity effects (buoyancy). With the quasi-hydrostatic approximation, the internal acoustic waves are removed completely. However, there still are external acoustic-like waves; e.g. the Lamb wave has  $m^2 = -\beta^2$  and  $\omega^2 = C_s^2 \kappa^2$  regardless of the value of  $a$ . The different wave-regimes are sketched in Fig. 6.1.

To further investigate the effects of the quasi-hydrostatic approximation on the dispersion of free waves, eq. (6.1) may be expressed in terms of the aspect ratio  $\alpha = H/L = k/m$ , where  $L$  and  $H$  are the horizontal and vertical scales of the motion. Hence,

$$\kappa^2 = \frac{\omega^2}{N^2} \cdot \left[ \beta^2 + \frac{N^2}{C_s^2} \left( 1 - a \frac{\omega^2}{N^2} \right) \right] / \left[ 1 - \frac{\omega^2}{N^2} \left( a + \frac{1}{\alpha^2} \right) \right] \quad (6.2)$$

Fig. 6.1 shows the dispersion for an infinite aspect ratio, representing the transition between internal and external waves; and for a finite, positive  $\alpha^2$ , representing internal waves. It is seen that the quasi-hydrostatic approximation seriously damages external waves of high frequency and short wavelength. The distortion decreases with increasing stability ( $N^2$ ). For internal waves ( $\alpha^2 > 0$  and finite) the distortion decreases remarkably for decreasing aspect ratio and increasing wavelength (see also Table 6.1). In a numerical model with chosen mesh width  $d$  one cannot resolve properly waves of shorter wavelength than  $\approx 5d$ . Based on Table 6.1 we will recommend the lower limit of the mesh width to be 1 km, as long as one is only interested to model internal gravity waves with aspect ratio smaller than unity.

Table 6.1: Angular frequency of free waves squared  $\omega^2$  ( $\text{s}^{-2}$ ) as a function of aspect ratio and wavelength. ( $N=0.01 \text{ s}^{-1}$ ,  $C_S=330 \text{ ms}^{-1}$ )

Type of solution	H/L = 1			H/L = 0.5			H/L = 0.1		
	$\lambda = 1 \text{ km}$	5 km	10 km	$\lambda = 1 \text{ km}$	5 km	25 km	$\lambda = 1 \text{ km}$	5 km	50 km
N.H. acoustic	8.599	$3.442 \times 10^{-1}$	$8.621 \times 10^{-2}$	21.50	$8.601 \times 10^{-1}$	$3.465 \times 10^{-2}$	434.2	17.37	$1.740 \times 10^{-1}$
N.H. gravity	$5.000 \times 10^{-5}$	$4.997 \times 10^{-5}$	$4.987 \times 10^{-5}$	$2.000 \times 10^{-5}$	$1.999 \times 10^{-5}$	$1.985 \times 10^{-5}$	$9.901 \times 10^{-7}$	$9.901 \times 10^{-7}$	$9.886 \times 10^{-7}$
QH	$9.999 \times 10^{-5}$	$9.984 \times 10^{-5}$	$9.937 \times 10^{-5}$	$2.500 \times 10^{-5}$	$2.499 \times 10^{-5}$	$2.475 \times 10^{-5}$	$1.000 \times 10^{-6}$	$1.000 \times 10^{-6}$	$9.984 \times 10^{-7}$

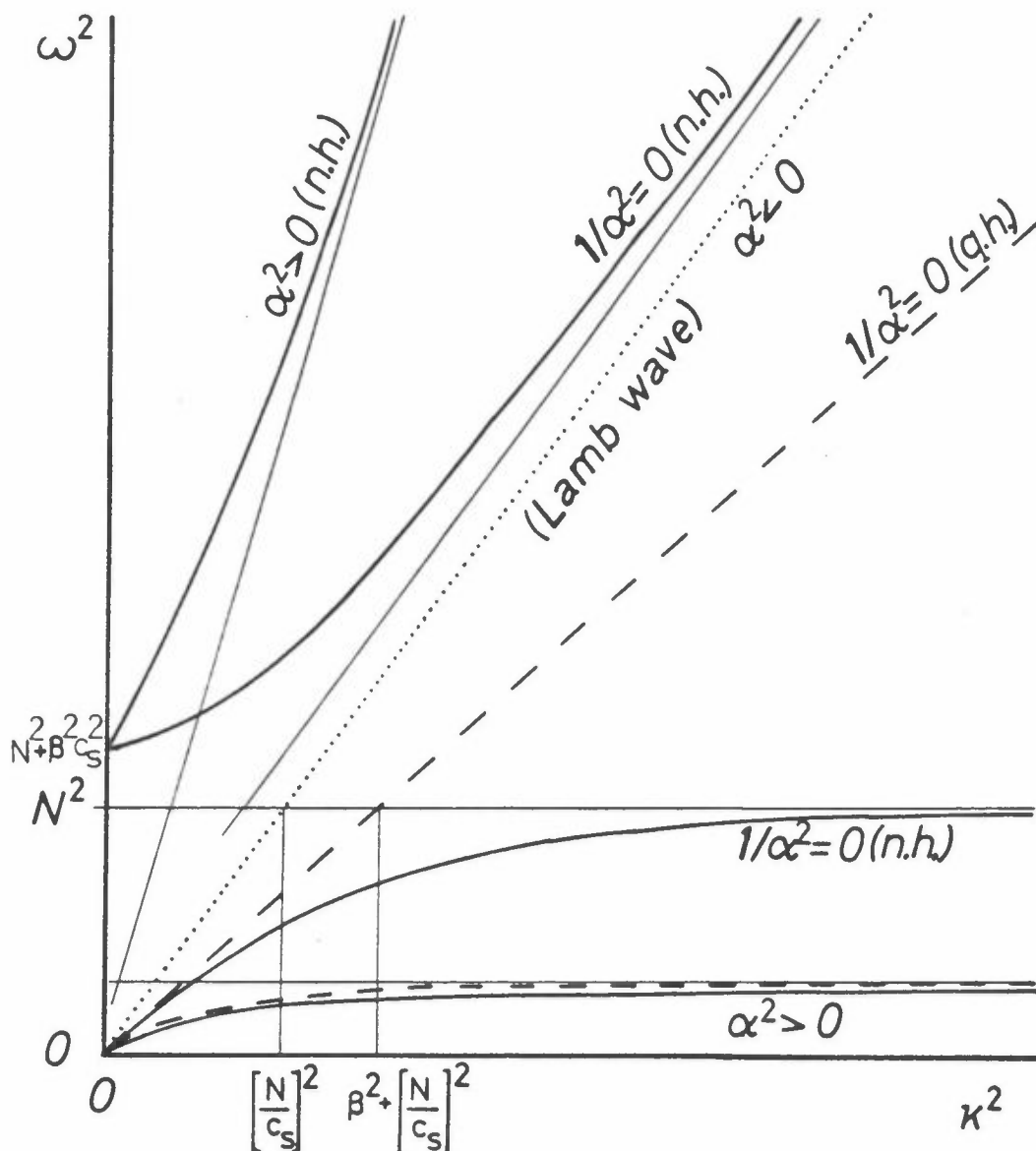


Figure 6.1: Dispersion diagram for free linear waves with neglected Coriolis terms. Continuous lines; non hydrostatic waves. Broken lines: Quasihydrostatic waves. Dotted line: the Lamb wave. See text for explanation of symbols.

### 6.1.2 Forced waves

The stationary, linear flow around an isolated mountain was investigated by Smith (1980). The mountain was assumed bell-shaped with scale  $a$ , and the Bouesinesq approximation was assumed. The basic state was a constant wind  $U$  and a constant Brunt-Väisälä frequency  $N$ . The condition for applying the quasi-hydrostatic approximation was deduced to be

$$\frac{Na}{U} \gg 1 \quad (6.3)$$

Assuming that the shortest mesh width which properly resolves the mountain is defined by  $5d = 2a$ , then the condition is

$$d \gg \frac{2}{5} \frac{U}{N} \quad (6.4)$$

Hence, if the sign ">>" signifies "greater than with at least a factor 5", then the mesh width  $d$  can be chosen as small as 1 km provided that the wind is so weak and the stability so strong that  $U/N \geq 500$  m. This is fulfilled with  $N=0.01 \text{ s}^{-1}$  and  $U = 5 \text{ ms}^{-1}$ , which are normal values in the atmosphere.

### 6.1.3 Forced circulation

Assuming an atmosphere over a flat earth with a horizontally varying surface temperature, Martin and Pielke (1983) investigated the applicability of the quasi-hydrostatic approximation. The solution of the equations linearized about a basic state at rest was found by the method of Defant (1950). In addition, the nonlinear equations were solved numerically, comparing the fully nonhydrostatic solution to the one obtained by imposing the quasi-hydrostatic approximation.

The main conclusion of the study was that a mesh width of 1.5 km or smaller may be appropriate in numerical models for sea-breezes over flat terrain which employs the quasi-hydrostatic approximation. The accuracy of the solution increases with increasing static stability and decreasing vertical turbulent exchange of heat.

#### 6.1.4 Unstable atmosphere

In all investigations regarding the applicability of the quasi-hydrostatic approximation, a result is that the quality of the quasi-hydrostatic solution increases with increasing static stability. This is not surprising, since a very stable atmosphere suppresses vertical motion and thus vertical accelerations. On the other hand, if the atmosphere turns unstable, vertical motion is reinforced so that the quasi-hydrostatic approximation should not be applied. This is indeed the case if the free solution of the equations linearized about a basic state at rest is considered. If acoustic waves are out of interest (which is normally the case), then the anelastic approximation can be made so that the term  $1/C_s^2$  can be removed from (6.1), giving

$$\omega^2 = N^2 \frac{\kappa^2}{a\kappa^2 + m^2 + \beta^2} \quad (6.5)$$

In the case of an unstable atmosphere,  $N^2 < 0$ , then  $\omega$  is imaginary and represents growth of convection cells. In the non-hydrostatic case, it is seen that  $|\omega^2| \rightarrow N^2$  when  $\kappa^2 \rightarrow \infty$ , while in the quasi-hydrostatic  $|\omega^2| \rightarrow \infty$  when  $\kappa^2 \rightarrow \infty$ . Thus, in the quasi-hydrostatic case the growth rate of convection increases beyond all limits with decreasing horizontal scale. In other words, the errors will be larger in a numerical model with a fine resolution than in a model with coarse. However, the horizontal extent of convective cells is so small that a mesh width smaller than 1 km is necessary for a proper resolution. The quasi-hydrostatic approximation can therefore not be applied in this case. Important to note here is that flows in cumulus clouds or moist unstable circulations within cloud layers are equally impossible to model by quasi-hydrostatic models. If such unstable flow is initiated in the model, the vertical sounding must be adjusted to be stable and the overall impacts of the flow parameterized. However, if a grid

which resolves the unstable circulations is used, one would then not achieve a solution which is representative for the resolved scale, but rather a kind of resulting mean state which is a characteristic for the flows on larger scales. It is therefore wasted resources to choose such a fine grid resolution when aiming at unstable cases with quasi-hydrostatic equations.

## 6.2 A SCALE ANALYSIS

In order to shed some more light on the validity of the quasi-hydrostatic approximation, a simple scale analysis of the vertical momentum equation is made. The equation, ignoring Coriolis terms, is

$$w_t + \vec{v} \cdot \nabla w + w w_z + \theta \Pi_z + g = \nabla \cdot [K_H \nabla w] + (K w_z)_z \quad (6.6)$$

where  $K_H$  is the horizontal exchange coefficient and  $K$  the vertical. Table 6.2 gives the order of magnitude of the different quantities employed in the equation. The horizontal scale is defined by the integer  $n$  ( $L \sim 10^n$ ) and the vertical velocity is made dependent on the stability and  $n$ . The smallest value of  $n$  which makes the non-hydrostatic terms substantially smaller than  $g$ , defines the lower limit of the applicability of the quasi-hydrostatic approximation.

Table 6.2: Order of magnitude of the quantities in eq. (6.6) ( $n$  is an integer number).

Variable	Symbol	Order of magnitude	
		Stable	Unstable
Horizontal scale	$L$	$10^n \text{ m}$	$10^n \text{ m}$
Vertical scale	$H$	$10^2 \text{ m}$	$10^3 \text{ m}$
Total atmospheric depth	$D$	$10^4 \text{ m}$	$10^4 \text{ m}$
Time scale	$T=L/U$	$10^{n-1} \text{ s}$	$10^{n-1} \text{ s}$
Potential temperature	$\Theta_o$	$10^2 \text{ K}$	$10^2 \text{ K}$
Exner function	$\Pi_o$	$10^3 \text{ m}^2 \text{ s}^{-2} \text{ K}^{-1}$	$10^3 \text{ m}^2 \text{ s}^{-2} \text{ K}^{-1}$
Horizontal flow	$U$	$10 \text{ ms}^{-1}$	$10 \text{ ms}^{-1}$
Vertical flow	$W$	$10^{2-n} \text{ ms}^{-1}$	$10^{3-n} \text{ ms}^{-1}$
Horizontal turbulent exchange	$K_{Ho}$	$10^{n-2} \text{ m}^2 \text{ s}^{-1}$	$10^{n-2} \text{ m}^2 \text{ s}^{-1}$
Vertical turbulent exchange	$K_{Ho}$	$1 \text{ m}^2 \text{ s}^{-1}$	$10^2 \text{ m}^2 \text{ s}^{-1}$

By scaling the each variable and letting a bar denote dimensionless quantities ( $\vec{v} = U \vec{\bar{v}}$  etc.), eq. (6.6) can be written in dimensionless form:

$$\begin{aligned}
 & \frac{\bar{w}}{t} + \vec{\bar{v}} \cdot \nabla \bar{w} + \frac{LW}{HU} \frac{\bar{w}\bar{w}}{z} + \frac{L\theta_0 \Pi_0}{UWD} \frac{\bar{\theta}\bar{\Pi}}{z} + \frac{L}{UW} g \\
 (1) \quad & \quad (1) \quad (10^{-1}) \quad \left( \begin{array}{c|c} 10^{2n-2} & 10^{2n-3} \\ \text{stable} & \text{unstable} \end{array} \right) \quad \left( \begin{array}{c|c} 10^{2n-2} & 10^{2n-3} \\ \text{stable} & \text{unstable} \end{array} \right) \\
 & = \frac{K_{Ho}}{UL} \vec{\bar{v}} \cdot (\bar{K}_H \vec{\bar{v}} \bar{w}) + \frac{LK_o}{UK^2} (\bar{K} \bar{w} \bar{z}) \bar{z} \quad (6.7) \\
 & \quad (10^{-3}) \quad (10^{n-5})
 \end{aligned}$$

The order of magnitude is denoted below each term. It is seen that even in the unstable case with the horizontal scale  $L=1$  km ( $n=3$ ), the non-hydrostatic terms are three orders of magnitude smaller than the gravity/vertical pressure gradient terms. This does not imply that the flow in an unstable atmosphere can be modelled explicitly by quasi-hydrostatic equations. As seen from the discussion in section 6.1.4, so called grid point overturning will be the result, since the growth rate of the convective cells will approach infinity as the horizontal scale approach zero. It is therefore assumed that the vertical sounding allways is adjusted to be stable. However, the values of vertical motion and turbulent exchange may be permitted to take values typically of an unstable atmosphere even for  $L=1$  km.

As a scale analysis is quite inaccurate, we will not recommend to simulate scales as small as 1 km with quasi-hydrostatic equations. Held together with the discussions of section 6.1, we arrive at the following smallest permitted grid increment. In an overall stable atmosphere with little moist acitivity, one can choose  $d \geq 1$  km. Examples of such simulations are drainage flows and other phenomena in the nocturnal boundary layer. (Winter time on high latitudes in areas under anticyclonic influence.) In a more general model aimed at simulating several kinds of mesoscale flows including moist circulations, the recommended grid increment is  $d \geq 5$  km. Such flows include coastal circulations, frontal rainbands, and mesoscale vortices.



## 7 EXAMPLES OF APPLICATIONS

The present model requires a significant amount of computer capacity. The computer facilities at DNMI (august 1986) consists of an FPS-164 array processor with core storage capacity of 1.024 MW of 64 bits, and an IBM 4341 front machine. A major part of these resources are well utilized by routine models on a daily basis, and there is at present no space left for routine modelling with the present mesoscale mesh. The work in this field is therefore presently restricted to case studies. In the following, results of three rather preliminary tests are shown. Basic data about the simulations are given in Table 7.1.

Table 7.1: Basic parameters for the model experiments.

	Coastal circulation	Gauss-mountain	Complex topography
Grid increment, $d$	10 km	3 km	1 km
Timestep, $\Delta t$	20 s	6 s	1.8 s
Latitude, $B$	$\sim 60^{\circ}$ N	$60^{\circ}$ N	$60^{\circ}$ N
Vertical layers, $K$	20	20	20
Pressure at top, $p_t$	300 hPa	300 hPa	300 hPa
Sea surface temp., $T_s$	$12^{\circ}$ C	-	$0^{\circ}$ C
Ground surface category	Bare earth	Bare earth	Bare earth/snow
Roughness param. $z_o$	$10^{-4}$ m(sea)/0.5 (land)	0.03 m	Horizontally variable
Initial state	Stable, calm atmosph. Rh = 60%	Stable, uniform wind $ \vec{v}  = 1.8 \text{ ms}^{-1}$ , Rh=60%	Taken from weather maps. Rh=60%

### 7.1 COASTAL CIRCULATION

Starting from a calm, stable atmosphere, the sun is rising above the horizon and heats the ground surface. Along a shoreline separating a sea surface with constant temperature from the ground surface, a sea breeze circulation is created. Figure 7.1 shows the wind along parts of the coastline after three hours of integration, at sigma-surfaces  $\sigma=0.98125$  ( $\approx 100$  m above ground) and  $\sigma=0.875$  ( $\approx 800$  m above ground). There is a well defined sea breeze circulation with maximum wind from the sea at the lowest level just on the landward side of the shore. There is a tendency towards an anticyclonic circulation over the sea,

and a cyclonic over the land. The compensating return current aloft is considerably weaker and has a tendency towards anticyclonic circulation over land and cyclonic over sea.

## 7.2 GAUSS-MOUNTAIN

The topography is constructed in order to study the flow around an isolated mountain. It is given by the formula

$$z_s(i,j) = \begin{cases} 0 & ; r > r_1 \\ H_0 \frac{\exp\left[\left(\frac{r}{r_0}\right)^2\right] - \exp\left[\left(\frac{r_1}{r_0}\right)^2\right]}{1 - \exp\left[\left(\frac{r_1}{r_0}\right)^2\right]} & ; r \leq r_1 \end{cases} \quad (7.1)$$

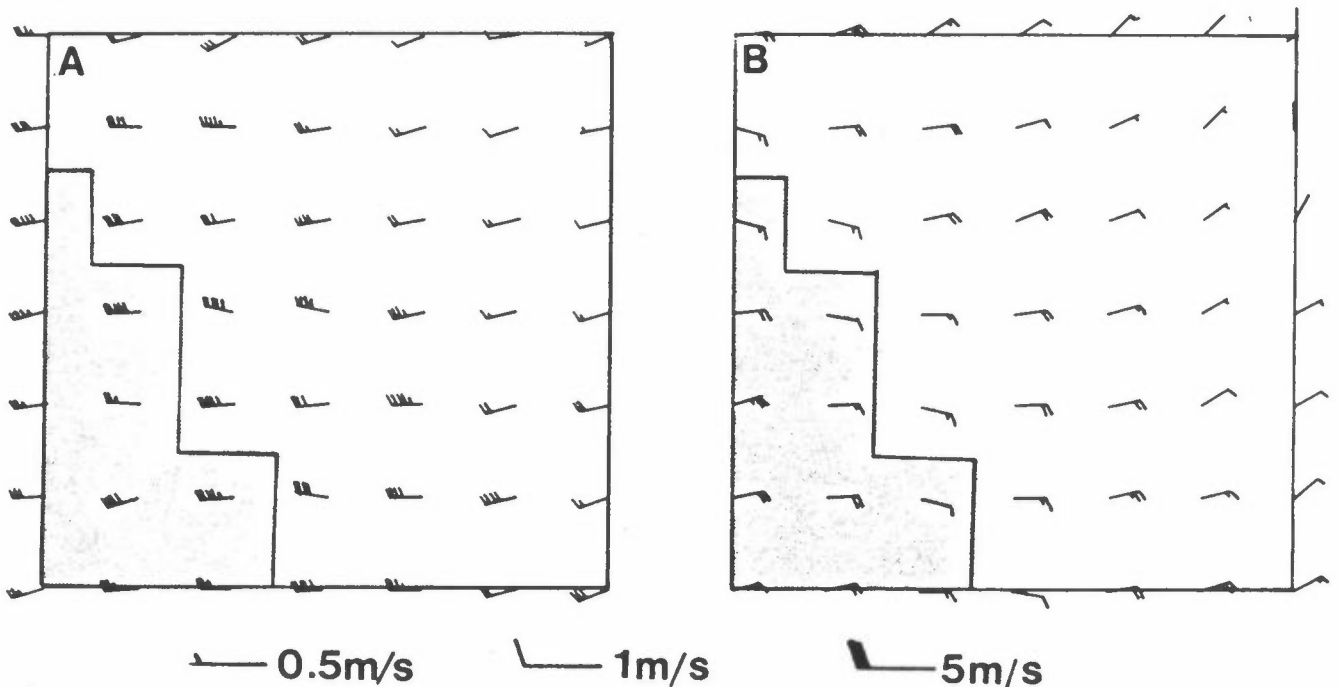


Figure 7.1: Results from coastal flow simulation. Section of central part of integration domain showing wind after three hours of integration. The sea surface is shaded.

a)  $\sigma = 0.98125$

b)  $\sigma = 0.875$

where  $r = [(i-i_0)^2 + (j-j_0)^2]^{1/2}$ ,  $r_0 = 7/3$ ,  $r_1 = 10/3$ ,  $i_0 = j_0 = 17$ ,  $H_0 = 1000$  m and  $(i,j)$  is a grid point. A homogeneous wind in geostrophic balance with the massfield and a stable atmosphere are the initial conditions. The ground surface properties are homogeneous, except for the topography. There is no solar heating. Results after one hour of integration are shown in Figs. 7.2a) and b), where b) is a vertical section along the line indicated on a). These figures can qualitatively be compared to the results of Smith (1980). Upwind of the mountain there is a split in the current into two branches on the sides of the two. A part of the air is also passing over the mountain, which is clearly indicated by the distortion of the isentropic surfaces. Potentially cold air is carried upslope on the upwind side and potentially warm air is carried downslope on the downwind side of the top. The maximum wind is found just over the top, which is consistent with the fact that the phase of a lee-wave slopes backwards into the deep atmosphere.

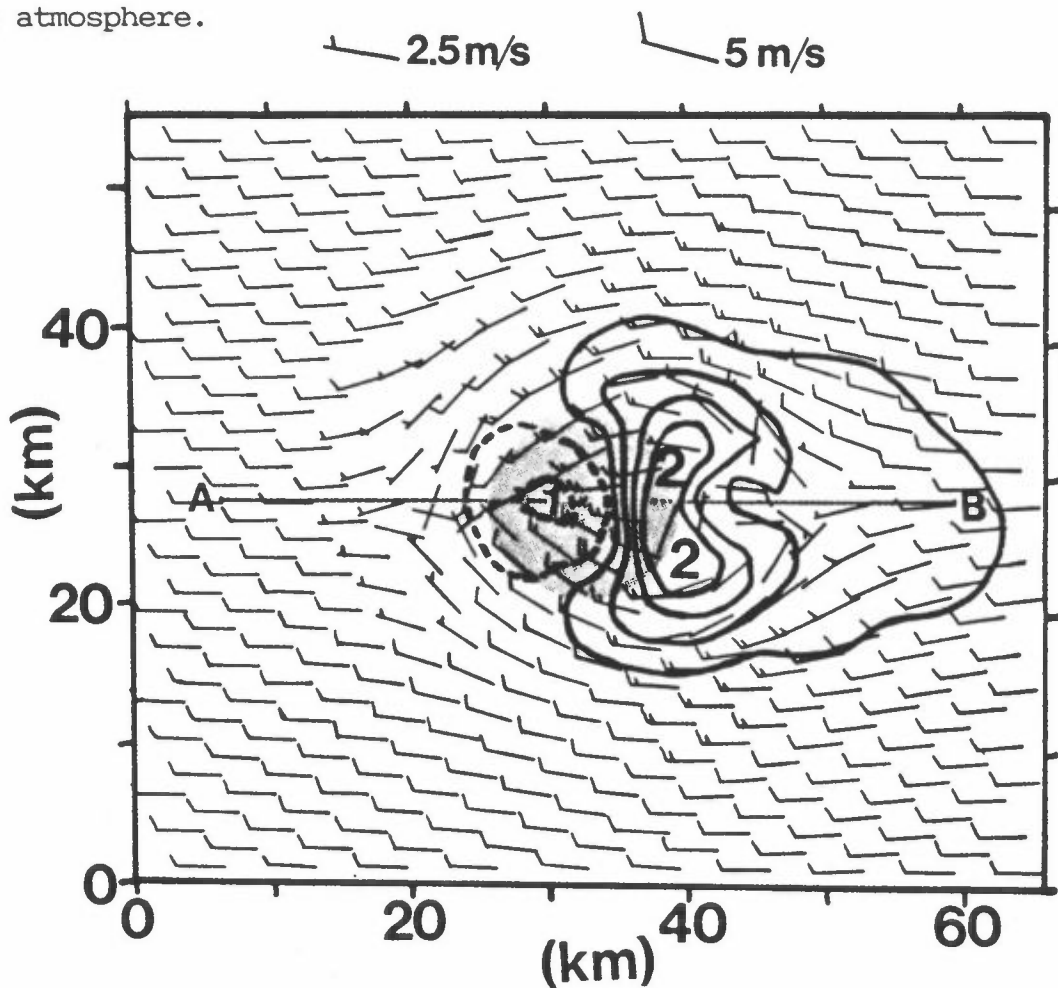


Figure 7.2: Result from Gaussian mountain simulation.

a) Section of integration domain after one hour of integration showing wind and change of potential temperature since  $t=0$  (unit  $10^{-1}K$ ), for  $\sigma=0.99875$ . The position of the mountain is indicated by a shaded circle.

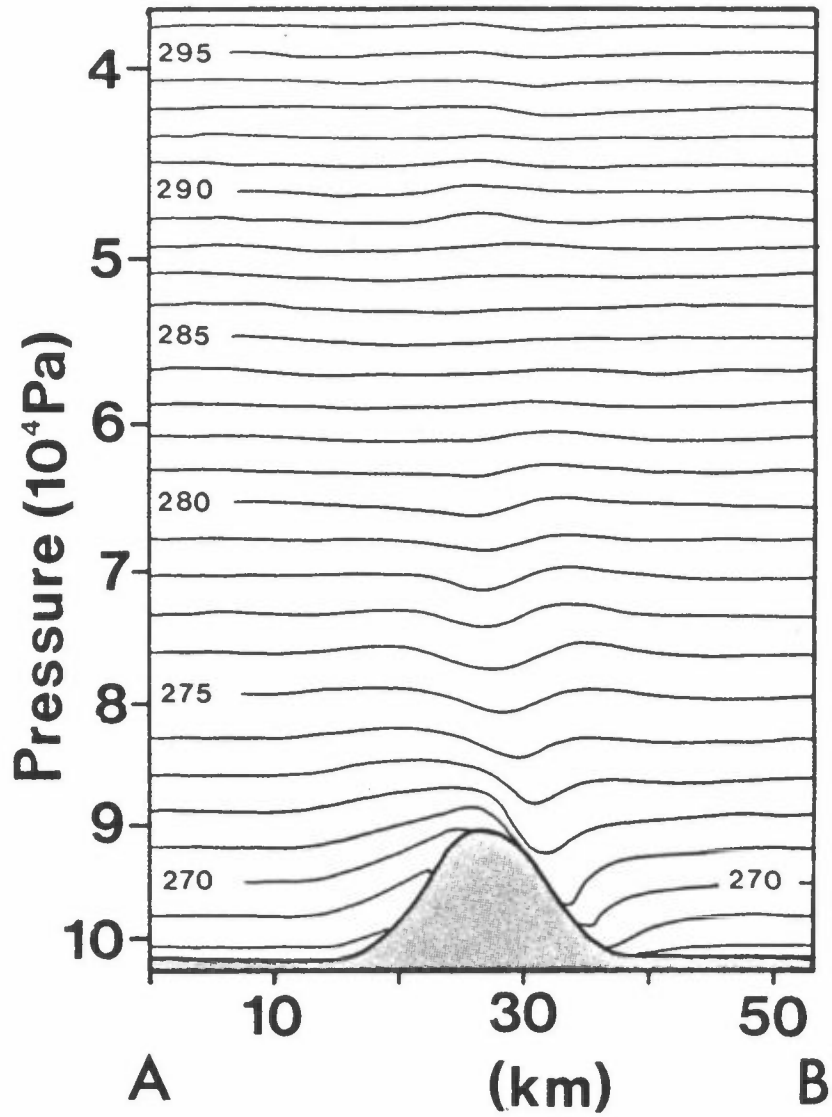


Figure 7.2: Result from Gaussian mountain simulation.

- b) Vertical section along the line indicated on a), showing potential temperature at intervals of 1 K after 1 h of integration.

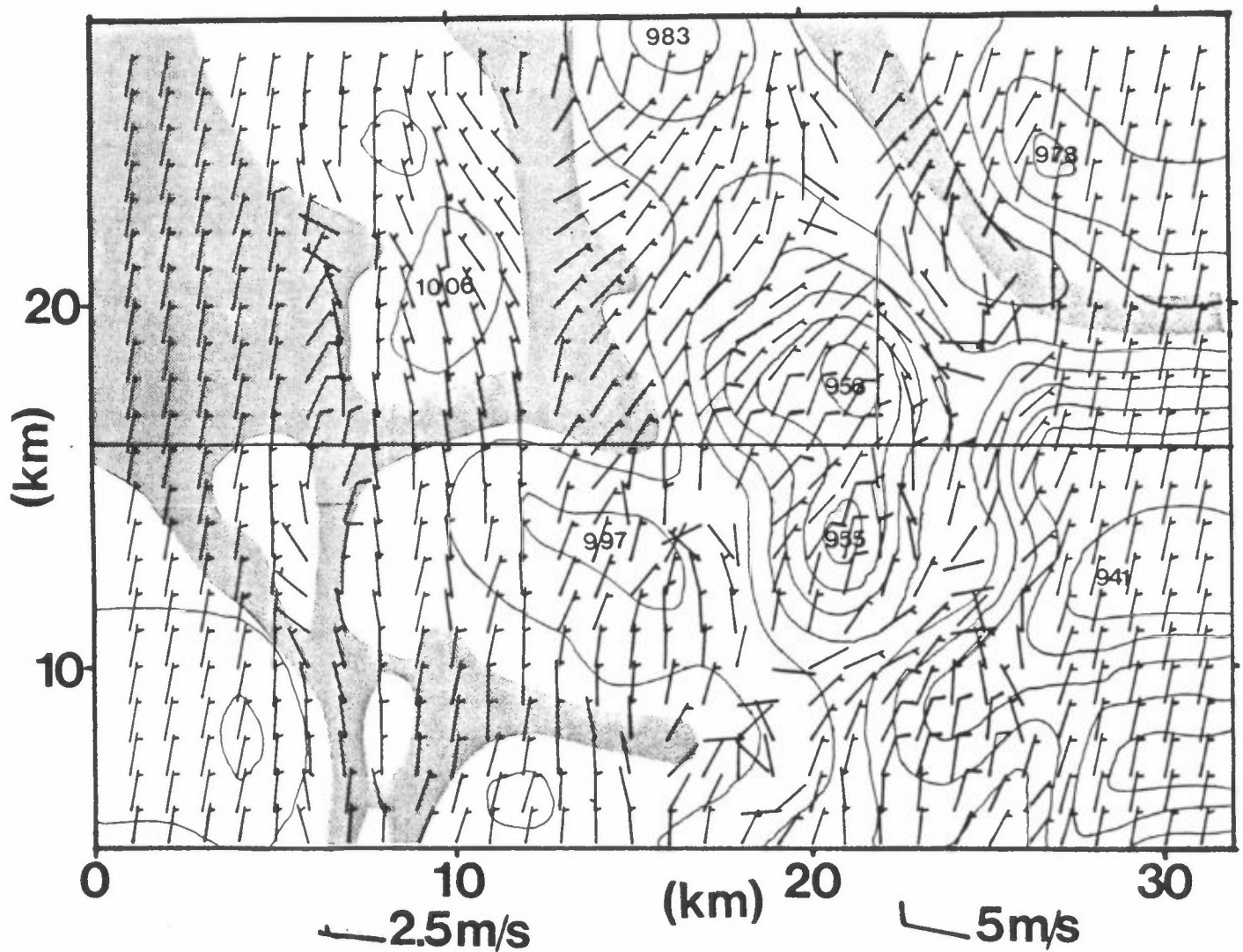


Figure 7.3: Results from complex terrain simulation.

a) Section of integration domain showing wind and surface pressure (in steps of 20 hPa) after 1 hour of integration. The fjords are indicated by shaded areas.

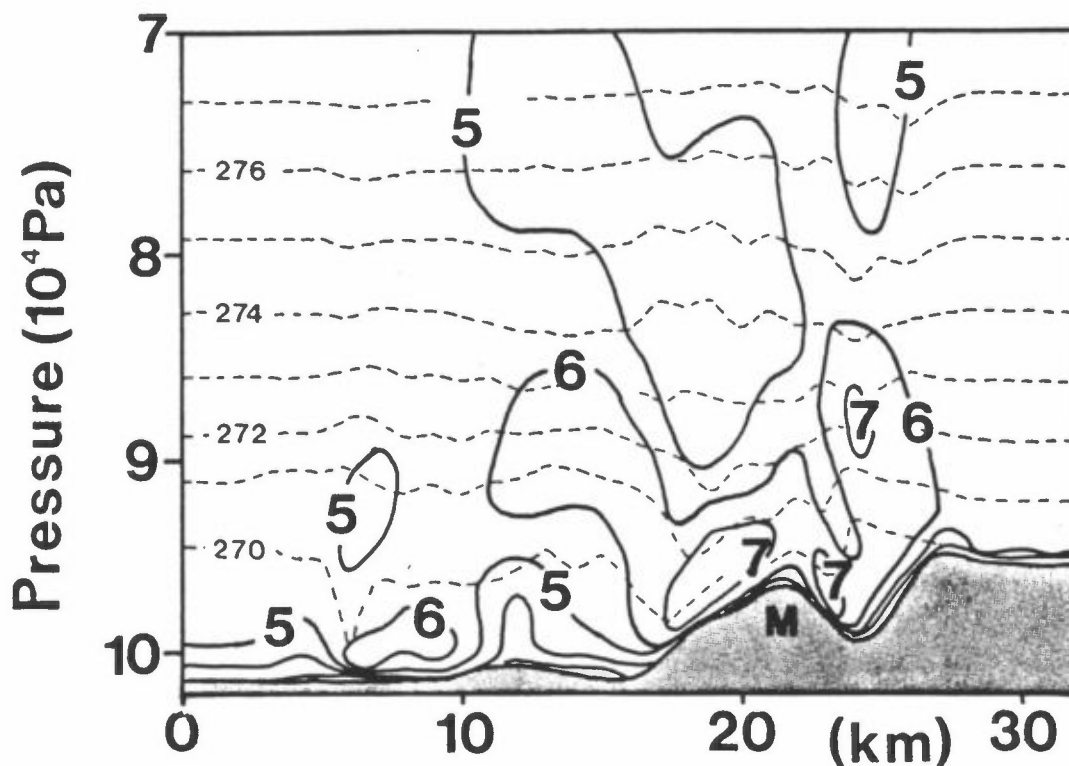


Figure 7.3: Results from complex terrain simulation.

- b) Vertical section of the lowermost 300 hPa along line indicated in a), showing potential temperature at intervals of 1 K (broken lines), and magnitude of wind component normal to the paper plane towards the reader at intervals of  $1 \text{ m/s}^{-1}$  (continuous lines). M indicates the position of the mountain referred to in the text.

### 7.3 COMPLEX TOPOGRAPHY

The last example of preliminary applications is a real-data simulation of wind in complex terrain. The actual area is the city and surroundings of Bergen on the western coast of Norway. This is an extremely complex site with respect to local meteorology. There are deep narrow valleys, in several cases with fjords that are year-around unfrozen, which separates mountains with heights over 1000 m. The city of Bergen is situated by a fjord in the bottom of such a valley. An example of wind modelling in this complicated geography, is shown in Fig. 7.3. The actual time was 20 Jan. 1986 01 local time. The initial conditions were taken from weather maps on the large scale. After one hour of integration, the winds had adjusted to the local forcing. The ground surface properties were highly inhomogeneous. The fjords were unfrozen with surface temperature  $0^{\circ}\text{C}$ , and the roughness length ranged from  $10^{-4}$  m over the sea to 0.5 m in the city center. The ground surface was considered as snow-covered above 300 m. (There was of course no sun heating.) From Fig. 7.3a) the effects of heating from the fjords as well as topographical steering are easily detected. At low levels, the wind blows from land out over the open sea. Fig. 7.3b) shows a vertical section along the line indicated on a). Considering the mountain marked with M on the figure, it is seen that the air current has split into two branches, one in each valley on the sides. Maximum wind speed is indeed experienced on each side of the top close to the ground surface.

## 8 REFERENCES

- Anthes, R.A. and Warner, T.T. (1978) Development of hydrodynamic models suitable for air pollution and other mesometeorological studies. Mon. Weather Rev., 106, 1045-1078.
- Birchfield, G.E. (1960) Numerical prediction of hurricane movement with use of a fine grid. J. Meteorol., 17, 406-414.
- Blackadar, A.K. (1979) High resolution models of the planetary boundary layer. Advances in Environment and Scientific Engineering, 1. Gordon and Branch, 276 pp.

- Bratseth, A. (1982) A simple and efficient approach to the initialization of weather prediction models. Tellus, 34, 352-357.
- Bratseth, A. (1983) Some economical, explicit finite-difference schemes for the primitive equations. Mon. Weather Rev., 111, 663-668.
- Brown, J.A. and Campana K.A. (1978) An economical time-differencing system for numerical weather prediction. Mon. Weather Rev., 106, 1125-1136.
- Businger, J.A. (1973) Turbulent transfer in the atmospheric surface layer. In: Workshop in micrometeorology, Chapter 2. Boston, Am. Meteorol. Soc.
- Businger, J.A., Wyngaard, J.C., Izumi, Y. and Bradley, E.F. (1971) Flux-profile relationship in the atmospheric boundary layer. J.Atmos.Sci., 28, 181-189.
- Carpenter, K.M. (1979) An experimental forecast using a non-hydrostatic mesoscale model. Quart. J. Roy. Meteorl. Soc., 105, 629-655.
- Charney, J.G., Fjørtoft, R. and von Neumann, J. (1950) Numerical integration of the barotropic vorticity equation. Tellus, 2, 237-254.
- Courant, R. and Hilbert, D. (1962) Methods of mathematical physics, Vol 2. New York Interscience Publishers.
- Davies, H.C. (1976) A lateral boundary formulation for multi-level prediction models. Quart. J. Roy. Meteorol. Soc., 102, 405-418.
- Davies, H.C. (1983) Limitations of some common lateral boundary schemes used in regional NWP models. Mon. Weather Rev., 111, 1002-1012.
- Deardorff, J.W. (1972) Parameterization of the planetary boundary layer for use in general circulation models. Mon. Weather Rev., 100, 93-106.
- Deardorff, J.F. (1978) Efficient prediction of ground surface temperature and moisture, with inclusion of a layer of vegetation. J. Geoph. Res., 83, No. C4, 1889-1903.
- Defant, F. (1950) Theorie der land - und seewind. Arch. Meteorol. Geophys. Bioklim., 2, 404-425.



- Drazin, P.G. and Howard, L.N. (1966) Hydrodynamic stability of parallel flows of inviscid fluid. Adv. Appl. Mech., 9, 1-89.
- Eliassen, A. (1983) Lectures on gravity waves in the atmosphere. In: Mesoscale Meteorology. Notes from a course on mesoscale meteorology held at Pinnarpsbaden, Sweden, 1983. (conducted by S. Bodin) SMHI, Sweden.
- Eliassen, A., and Pedersen, K. (1977) Meteorology, an Introductory Course. Vol. II. Oslo, Universitetsforlaget, pp. 38-42.
- Grandin, G. (1983) A one-dimensional PBL model with a subgrid scale condensation scheme for stratiform clouds and fog. Uppsala, Meteorologiska Institutionen, Kungliga Universitet (Reports No. 72).
- Grønås, S. and Hellevik, O.E. (1982) A limited area prediction model at the Norwegian Meteorological Institute. Oslo. The Norwegian Meteorological Institute (Techn. Rep. No. 61).
- Hill, G.E. (1968) Grid telescoping in numerical weather prediction. J. Appl. Meteorol., 7, 29-38.
- Janjic, Z.I. (1977) Pressure gradient force and advection scheme used for forecasting with steep and small scale topography. Contrib. Atmos. Phys., 50, 186-199.
- Jacobs, C.A., Pandolfo, J.P. and Atwarer, M.A. (1974) A description of a general three dimensional numerical simulation model of a coupled air-water and/or air-land boundary layer. Center for the Environment and Man, Hartford, Conn. (IFYGL, Final Report, CFM, Rep. Nos. 5131-509a).
- Kondratyev, J. (1969) Radiation in the atmosphere. Academic press. pp. 187-202.
- Koss, W. (1971) Numerical integration experiments with variable resolution, two dimensional cartesian grids using box methods. Mon. Weather Rev., 99, 725-738.
- Kuo, H.L. (1965) On formation and intensification of tropical cyclones through latent heat release by cumulus convection. J. Atmos. Sci., 22, 40-63.
- Kuo, H.L. (1974) Further studies of the parameterization of the influence of cumulus convection on large-scale flow. J. Atmos. Sci., 31, 1232-1240.

- Källberg, P. and Gibson, J.K. (1977) Lateral boundary conditions for a limited area version of ECMWF model. Geneva, WMO (WGNE Progress Report No. 14). pp. 103-105.
- Louis, J.F. (1979) A parametric model of vertical eddy fluxes in the atmosphere. Boundary Layer Meteorol., 17, 187-202.
- Manabe, S., Smagorinski, J. and Strickler, R.F. (1965) Simulated climatology of a general circulation model with a hydrological cycle. Mon. Weather Rev., 89, 503-532.
- Martin, C.L. and Pielke, R.A. (1983) The adequacy of the hydrostatic assumption in sea breeze modelling over flat terrain. J. Atmos. Sci., 40, 1472-1481.
- McDonald, J.E. (1960) Direct absorption of solar radiation by atmospheric water vapor. J. of Meteorol., 17, 319.
- McNider, R.T. and Pielke, R.A. (1981) Diurnal boundary-layer development over sloping terrain. J. Atmos. Sci., 38, 2198-2212.
- McPherson, R.D. (1970) A numerical study of the effect of a coastal irregularity on the sea breeze. J. Appl. Meteorol., 9, 767-777.
- Mellor, G.L. and Yamada, T. (1974) A hierarchy of turbulence closure models for planetary boundary layers. J. Atmos. Sci., 1791-1806.
- Mesinger, F. and Janjic, Z.I. (1983) Finite-difference schemes for the pressure gradient force and for the hydrostatic equation. In: Numerical methods for weather prediction, Vol. I. Seminar held at ECMWF, 1983. pp. 103-157.
- O'Brien, J.J. (1970) A note on the vertical structure of the eddy exchange coefficient in the planetary boundary layer. J. Atmos. Sci., 27, 1213-1215.
- Ookochi, Y. (1972) A computational scheme for the nesting of a fine mesh in the primitive equation model. J. Meteorol. Soc. Japan, 50, 37-48.
- Phillips, N.A. and Shukla, J. (1973) On the strategy of combining coarse and fine grid meshes in numerical weather prediction. J. Appl. Meteorol., 12, 763-770.
- Pielke, R.A. (1974) A three-dimensional model for the sea breezes over south Florida. Mon. Weather Rev., 102, 115-139.

Potter, D. (1983) Computational physics, John Wiley and Sons Ltd.  
pp. 88-101.

Shapiro, M.A. and O'Brien, J.J. (1970) Boundary conditions for fine-mesh limited area forecasts. J. Appl. Meteorol., 9, 345-349.

Smith, R.B. (1980) Linear theory of stratified hydrostatic flow past an isolated mountain. Tellus, 32, 348-364.

Stephens, G.L. (1948) The parameterization of radiation for numerical weather prediction and climate models. Mon. Weather Rev., 112, 826-867.

Sundqvist, H. (1975) On truncation errors in sigma-system models. Atmosphere, 13, 81-85.

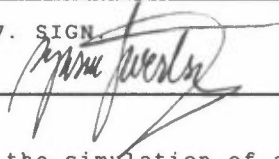
Sundstrom, A. and Elvius, T. (1979) Computational problems related to limited area modelling. In: Numerical methods used in atmospheric models, Vol. 2. Geneva, WMD (GARP publication series No. 17). pp. 379-416.

Tapp, M.C. and White, P.W. (1976) A non-hydrostatic mesoscale model. Quart. J. Roy. Meteorol. Soc., 102, 277-296.

Wang, H.-H. and Halpern, P. (1970) Experiments with a regional fine-mesh prediction model. J. Appl. Meteorol., 9, 545-553.

Økland, H. (1972) On a balance, initialization and data assimilation in primitive equation prediction models. J. Atmos. Sci., 29, 641-648.

NORSK INSTITUTT FOR LUFTFORSKNING (NILU)  
 NORWEGIAN INSTITUTE FOR AIR RESEARCH  
 POSTBOKS 64, N-2001 LILLESTRØM

RAPPORTTYPE TECHNICAL REPORT	RAPPORTNR. TR 2/87	ISBN-82-7247-813-7	
DATO FEBRUAR 1987	ANSV. SIGN. 	ANT. SIDER 66	PRIS NOK 60.-
TITTEL A numerical model suitable for the simulation of a broad class of circulation systems on the atmospheric mesoscale.		PROSJEKTLEDER Trond Iversen	
		NILU PROSJEKT NR. E-8263	
FORFATTER(E) Trond Iversen and Thor Erik Nordeng		TILGJENGELIGHET A	
		OPPDRAGSGIVERS REF.	
OPPDRAGSGIVER (NAVN OG ADRESSE) Norsk institutt for luftforskning			
3 STIKKORD (à maks. 20 anslag) Mesoscale                      Modelling                      Atmosphere			
REFERAT (maks. 300 anslag, 7 linjer)			

TITLE
ABSTRACT (max. 300 characters, 7 lines) The report constitutes a documentation of a numerical model for the atmospheric mesoscale. The model includes a high resolution planetary boundary layer parameterization, an equation for ground surface temperature and a full scheme for humidity. Long wave radiation is also included. The model is designed to be nested into models on larger scales. A few examples of application are included.

\* Kategorier: Åpen - kan bestilles fra NILU                      A  
                   Må bestilles gjennom oppdragsgiver                    B  
                   Kan ikke utleveres    C